Nucleation Processes in Deep Convection Simulated by a Cloud-System-Resolving Model with Double-Moment Bulk Microphysics

VAUGHAN T. J. PHILLIPS

Atmospheric and Oceanic Sciences Program, Princeton University, Princeton, New Jersey

LEO J. DONNER AND STEPHEN T. GARNER

NOAA/Geophysical Fluid Dynamics Laboratory, Princeton, New Jersey

(Manuscript received 2 December 2005, in final form 15 July 2006)

ABSTRACT

A novel type of limited double-moment scheme for bulk microphysics is presented here for cloud-system-resolving models (CSRMs). It predicts the average size of cloud droplets and crystals, which is important for representing the radiative impact of clouds on the climate system. In this new scheme, there are interactive components for ice nuclei (IN) and cloud condensation nuclei (CCN). For cloud ice, the processes of primary ice nucleation, Hallett–Mossop (HM) multiplication of ice particles (secondary ice production), and homogeneous freezing of aerosols and droplets provide the source of ice number. The preferential evaporation of smaller droplets during homogeneous freezing of cloud liquid is represented for the first time. Primary and secondary (i.e., in cloud) droplet nucleation are also represented, by predicting the supersaturation as a function of the vertical velocity and local properties of cloud liquid. A linearized scheme predicts the supersaturation, explicitly predicting rates of condensation and vapor deposition onto liquid (cloud liquid, rain) and ice (cloud ice, snow, graupel) species. The predicted supersaturation becomes the input for most nucleation processes, including homogeneous aerosol freezing and secondary droplet activation.

Comparison of the scheme with available aircraft and satellite data is performed for two cases of deep convection over the tropical western Pacific Ocean. Sensitivity tests are performed with respect to a range of nucleation processes. The HM process of ice particle multiplication has an important impact on the domain-wide ice concentration in the lower half of the mixed-phase region, especially when a lack of upper-level cirrus suppresses homogeneous freezing. Homogeneous freezing of droplets and, especially, aerosols is found to be the key control on number and sizes of cloud particles in the simulated cloud ensemble. Preferential evaporation of smaller droplets during homogeneous freezing produces a major impact on ice concentrations aloft. Aerosols originating from the remote free troposphere become activated in deep convective updrafts and produce most of the supercooled cloud droplets that freeze homogeneously aloft. Homogeneous aerosol freezing is found to occur only in widespread regions of weak ascent while homogeneous droplet freezing is restricted to deep convective updrafts. This means that homogeneous aerosol freezing can produce many more crystals than homogeneous droplet freezing, if conditions in the upper troposphere are favorable.

These competing mechanisms of homogeneous freezing determine the overall response of the ice concentration to environmental CCN concentrations in the simulated cloud ensemble. The corresponding sensitivity with respect to environmental IN concentrations is much lower. Nevertheless, when extremely high concentrations of IN are applied, that are typical for plumes of desert dust, the supercooled cloud liquid is completely eliminated in the upper half of the mixed phase region. This shuts down the process of homogeneous droplet freezing.

Corresponding author address: Vaughan T. J. Phillips, Dept. of Meteorology, University of Hawaii at Manoa, 2525 Correa Rd., Honolulu, HI 96822.
E-mail: vaughanp@hawaii.edu

DOI: 10.1175/JAS3869.1

1. Introduction

Clouds are a major control on the fluxes of shortwave and longwave radiation throughout the atmosphere. The immediate radiative impact of a cloud depends on the average size of its particles and its mass of liquid and ice. Particle sizes also can influence its lifetime and spatial extent through the preferential sedimentation of larger particles and through the coagulation of cloud particles to form precipitation. In bulk microphysics schemes of cloud-system-resolving models (CSRMs), prediction of the number of droplets and crystals as advected quantities allows their sizes to be predicted, for an assumed form of the particle size distribution. Such schemes are referred to as double moment.

Double-moment bulk schemes represent the many mechanisms by which cloud particles are formed. These nucleation pathways are especially diverse for ice. Homogeneous freezing is the type of ice nucleation that occurs by the spontaneous freezing of supercooled cloud droplets or aerosols at temperatures below about −36°C, without the action of ice nuclei. Heterogeneous freezing is the type of ice nucleation that does involve the action of an ice nucleus. Furthermore, emission of fragments of ice during collisions yields extra crystals (ice particle multiplication). Nucleation of droplets occurs at cloud base, where there is a peak of supersaturation (primary droplet nucleation), but also may happen in the interior of the cloud (in-cloud or secondary droplet nucleation).

Entrainment of midlevel aerosols into a rapid cumulonimbus updraft observed in the Cirrus Regional Study of Tropical Anvils and Cirrus Layers-Florida Area Cirrus Experiment (CRYSTAL-FACE) was found to be critical in the generation of anvil ice particles in simulations with a 3D cloud model with spectral microphysics by Fridlind et al. (2004). Phillips et al. (2005) and Heymsfield et al. (2005) explained this result in terms of elimination of primary droplets from cloud base by accretion onto precipitation and high supersaturations in rapid updrafts aloft, causing in-cloud droplet nucleation and homogeneous droplet freezing. Heymsfield et al. (2005) claimed that, in weaker convective updrafts with speeds less than a few meters per second, cloud liquid evaporates without freezing homogeneously. This then opens up the possibility that either heterogeneous ice nucleation or homogeneous aerosol freezing may prevail in the formation of ice over regions of weak ascent in cirrus away from cores of deep convection.

An area of uncertainty appears to be how such conclusions about nucleation, obtained from studies of individual cells of deep convection, apply at the scale of an entire cloud ensemble. The motivation for studying nucleation in convection over a domain of this scale is that it encompasses many types of cloud, and it is the scale of a grid box in a general circulation model (GCM). Currently, there is much interest in prediction of cloud particle numbers in GCMs with a goal of predicting the radiative properties of clouds and aerosol–cloud interactions.

Consequently, the aim of the present paper is to assess the roles of the myriad of nucleation processes for cloud particles in a cloud ensemble. This is done with a new parameterization of double-moment bulk microphysics in a CSRM. There are the following distinctive aspects of this bulk microphysics scheme presented here. 1) In-cloud droplet nucleation is rigorously represented by prediction of the in-cloud supersaturation with a novel linearized supersaturation scheme and from the interactive component of soluble aerosol. There is no saturation adjustment. 2) Diffusional growth is evaluated explicitly by the linearized scheme. 3) A parameterization of small-droplet evaporation during episodes of homogeneous droplet freezing at −36°C, which is not found in any other bulk microphysics scheme, has been innovated here. 4) There is application of recent in situ data of the activity of ice nuclei at temperatures colder than −30°C. 5) Homogeneous aerosol freezing is represented by the recent theory from Koop et al. (2000). 6) Mathematical forms of cloud-particle size distributions are constrained by aircraft observations, partly analyzed in the present study. 7) Fall speeds for cloud-ice include a dependence on their predicted average size, based on laboratory observations. 8) The autoconversion formula for the warm rain process presented by Lin et al. (1983) is modified, introducing a dependence of its threshold on predicted droplet number and relative dispersion of the droplet size distribution. 9) There is a double-moment representation applied to both cloud ice and cloud liquid, in contrast with most other double-moment microphysics schemes (e.g., Ziegler 1985; Cotton et al. 1986; Chaumerliac et al. 1987; Ikawa et al. 1991; Ferrier 1994; Harrington et al. 1995; Meyers et al. 1997; Reisner et al. 1998; Swann 1998a,b; Cohard and Pinty 2000; Khairoutdinov and Kogan 2000; Chen and Liu 2004). A minority of bulk microphysics schemes do apply a double-moment representation to both of these species (e.g., Levkov et al. 1992; Wang and Chang 1993; Girard and Curry 2001; Cotton et al. 2003; Saleeby and Cotton 2004; Morrison et al. 2005; Seifert and Beheng 2005), but the present scheme differs from these in ways noted above.

The new double-moment bulk microphysics scheme is described in the next section. Results for simulations

of periods from two tropical oceanic cases are presented, in comparison with aircraft and satellite observations. These are the Tropical Ocean Global Atmosphere Coupled Ocean–Atmosphere Response Experiment (TOGA COARE; 20–26 December 1992) and the Kwajalein Experiment (KWAJEX; 17–31 August 1999). TOGA COARE took place at the western edge of the Pacific Ocean, while KWAJEX occurred near the Kwajalein Atoll in the Republic of the Marshall Islands in a more remote part of the Pacific (Kummerow et al. 2000). This validation is much more comprehensive than for most other double-moment schemes. To initialize the model, prescribed cloud condensation nuclei (CCN) profiles are applied that are consistent with aircraft observations from the tropical Pacific Ocean (Clarke and Kapustin 2002). The relative roles of various nucleation processes are outlined in sections 5 and 6. Conclusions are presented in section 7.

2. Description of double-moment microphysics scheme

a. Overview

The bulk microphysics parameterization has five classes of hydrometeor (cloud liquid, cloud ice, snow, graupel, and rain), and includes sedimentation of cloud ice and cloud liquid. There are interactive components for the aerosol activity spectra.

The size distributions of cloud ice and cloud liquid ($x = w, i$) obey a gamma law:

$$n(D_x) = n_{x,0} D_x^{p_x} \exp(-\lambda_x D_x), \tag{1}$$

where D_x is the equivalent spherical diameter (m) and $n(D_x)dD_x$ is the number concentration (m^{-3}) of particles in the size range dD_x. Also, λ_x (m^{-1}) is the slope, $n_{x,0}$ is the intercept ($m^{-(4+p_x)}$), and p_x is the shape parameter of the distribution. For cloud ice, p_i is set to unity since this was found to be the value needed to fit size distributions of small crystals in aircraft observations from the Central Equatorial Pacific Experiment (CEPEX) analyzed by McFarquhar and Heymsfield (1997). For cloud water, p_w is set to 3.5, based on an analysis of aircraft data from the Forward Scattering Spectrometer (FSSP) and two-dimensional cloud (2D-C) probes of droplet size distributions in deep convection above the freezing level during CRYSTAL-FACE (18 July 2002). Its value is within the range of values from a variety of previous observational studies (Tampieri and Tomasi 1976) and corresponds to a relative dispersion (ratio of the standard deviation to the mean of the diameter) of 0.47, which also is within the typical range of observed values (Twomey 1966).

The number and mass mixing ratios of cloud liquid and cloud ice (kg^{-3}) are

$$n_x = \int_0^\infty n(D_x)\, dD_x/\rho_a \tag{2}$$

$$q_x = \rho_x \frac{\pi}{6} \int_0^\infty D_x^3 n(D_x)\, dD_x/\rho_a, \tag{3}$$

where the mass of a given particle is $m_x = \rho_x(\pi/6)D_x^3$, with ρ_x (kg m^{-3}) being the bulk density of the particle and ρ_a (kg m^{-3}) being the air density. This yields

$$\lambda_x = \left[\frac{\Gamma(4 + p_x)\rho_x \frac{\pi}{6} n_x}{\Gamma(1 + p_x) q_x} \right]^{1/3}. \tag{4}$$

Also, $n_{x,0} = (n_x \rho_a)\lambda_x^{1+p_x}/\Gamma(1 + p_x)$. Here, Γ is the Gamma function. For cloud ice particles, owing to their small size (<100 μm at most levels), a bulk density close to that of pure ice is assumed (ρ_i = 900 kg m^{-3}), which is consistent with aircraft observations of small crystals in tropical cirrus over the equatorial Pacific (McFarquhar et al. 1999) and in anvil cirrus over Florida in CRYSTAL-FACE (Heymsfield et al. 2004).

For snow, graupel, and rain ($x = s, g, r$), the exponential form of the size distribution in the scheme by Lin et al. (1983) is retained, except that the intercept value, $n_{s,0}$ (m^{-4}), of snow is based on aircraft observations of tropical deep convection. This single-moment treatment of precipitation reduces the computational expense of the scheme. Analysis of aircraft data from the KWAJEX (Heymsfield et al. 2002) for the only day when upper-level cirrus was present (22 August 2002) yields a value of $n_{s,0} = 3 \times 10^7$ m^{-4} for an assumed average size of snow particles of 0.5 mm, a value slightly larger than the autoconversion threshold for generation of snow by cloud ice in the model. Inspection of a composite size distribution containing cloud ice and snow observed in CEPEX at the lowest observational level presented by McFarquhar et al. (1999) yields the same value of $n_{s,0}$ if snow is assumed to govern the size distribution at sizes >0.5 mm.

The bulk microphysics parameterization follows Lin et al. (1983) (see Lord et al. 1984) except for the following modifications. 1) Numbers of particles of cloud liquid and cloud ice are predicted. 2) An empirical value for $n_{0,s}$ based on aircraft observations is introduced (a single-moment approach is still applied for all precipitation). 3) No saturation adjustment or parameterization of the Bergeron–Findeisen process is applied, since diffusional growth of cloud particles and precipitation is now simulated explicitly with a linearized supersaturation scheme. 4) Sedimentation of cloud

particles has been introduced. 5) Freezing of all supercooled rain is performed at −35°C. 6) Homogeneous freezing of supercooled cloud liquid allows for evaporation of a fraction of its mass without freezing. 7) Autoconversion of cloud liquid to rain depends on the mean droplet size implied by the predicted droplet number (and similarly for the autoconversion of cloud ice to snow) and on the width of the droplet size distribution. 8) Conversion of snow to graupel by riming has been expressed in terms of the riming rate. 9) Accretion of particles of cloud liquid and cloud ice represents, to a degree, the dependence of collision efficiency on their size. The linearized scheme that predicts the in-cloud supersaturation and diffusional growth of cloud particles is described in the appendix.

b. Continuity equations

The prognostic equations for the (mass) mixing ratios of vapor, cloud liquid, and cloud ice within the bulk microphysics parameterization are

$$\frac{dq_v}{dt} = \mathrm{Ev}_{\mathrm{hom}}(q_v; q_w) - [\mathrm{Fr}(q_i; \mathrm{CCN}) + \mathrm{De}(q_i; q_v|\mathrm{IN}) + \mathrm{Co}(q_w; q_v|\mathrm{CCN}) + \sum_{x=w,r} \mathrm{Co}(q_x; q_v) + \sum_{x=i,s,g} \mathrm{De}(q_x; q_v)] \quad (5)$$

$$\frac{dq_w}{dt} = \mathrm{Co}(q_w; q_v|\mathrm{CCN}) + \mathrm{Co}(q_w; q_v) + \mathrm{Me}(q_w; q_i) - [\mathrm{Au}(q_r; q_w|q_w) + \sum_{X=\mathrm{IN,CIN}} \mathrm{Fr}(q_i; q_w|X) + \mathrm{Ev}_{\mathrm{hom}}(q_v; q_w) + \mathrm{Fr}(q_i; q_w) + \sum_{x=r,g,s} \mathrm{Ac}(q_x; q_w)|q_x + \mathrm{Ac}(q_x; q_w|q_i)] \quad (6)$$

$$\frac{dq_i}{dt} = \mathrm{De}(q_i; q_v|\mathrm{IN}) + \mathrm{De}(q_i; q_v) + \sum_{X=\mathrm{IN,CIN}} \mathrm{Fr}(q_i; q_w|X) + \sum_{x=s,g} \mathrm{HM}(q_i; q_w|q_x) + \sum_{X=q_w,\mathrm{CCN}} \mathrm{Fr}(q_i; X) - [\mathrm{Au}(q_s; q_i|q_i) + \sum_{x=s,g} \mathrm{Ac}(q_x; q_i|q_x) + \gamma_i \mathrm{Ac}(q_g; q_r|q_i) + \mathrm{Me}(q_w; q_i)]. \quad (7)$$

Table 1 defines symbols for microphysical conversion terms, IN is ice nuclei, and CIN is contact ice nuclei. Here, γ_i is the fractional contribution to the production rate of graupel mass, by collisional raindrop freezing, arising from the mass of the accreted cloud ice only. All source terms not described in the present text, and the prognostic equations for mass mixing ratio of rain, snow, and graupel, are as described by Lin et al. (1983). The corresponding prognostic equations for particle number mixing ratios are

$$\frac{dn_w}{dt} = \mathrm{Co}(n_w; q_v|\mathrm{CCN}) + \mathrm{Me}(n_w; n_i) - [\mathrm{Au}(n_r; n_w|n_w) + \sum_{X=\mathrm{IN,CIN}} \mathrm{Fr}(n_i; n_w|X) + \mathrm{Ev}_{\mathrm{hom}}(q_v; n_w) + \mathrm{Fr}(n_i; n_w) + \sum_{x=r,g,s} \mathrm{Ac}(n_x; n_w|n_x) + \mathrm{Ac}(n_s; n_w|n_i) + \mathrm{Ev}(q_v; n_w)] \quad (8)$$

$$\frac{dn_i}{dt} = \mathrm{De}(n_i; q_v|\mathrm{IN}) + \sum_{X=\mathrm{IN,CIN}} \mathrm{Fr}(n_i; n_w|X) + \sum_{x=s,g} \mathrm{HM}(n_i; n_w|n_x) + \sum_{x=n_w,\mathrm{CCN}} \mathrm{Fr}(n_i; x) - [\mathrm{Au}(n_s; n_i|n_i) + \sum_{x=s,g} \mathrm{Ac}(n_x; n_i|n_x) + \mathrm{Ac}(n_g; n_i|n_r) + \mathrm{Me}(n_w; n_i) + \mathrm{Su}(q_v; n_i)], \quad (9)$$

where Su is sublimation.

Additionally, there are two further prognostic equations for number mixing ratios of activated CCN and IN (see section 2c). Full evolution equations for mass and number mixing ratio include advective, turbulent, and precipitation flux tendencies, in addition to the microphysical tendencies given here and are described by Ferrier (1994). Note that the number mixing ratios, n_x, of precipitation species are diagnosed from prescribed values of $n_{0,x}$ (a single-moment approach).

c. Aerosol activity spectra

A power-law activity spectrum of CCN is applied for droplet nucleation. The number of CCN, N_{CCN} (m^{-3}), activated at supersaturation, s (%), is

$$N_{\mathrm{CCN}} = Cs^k, \quad (10)$$

where C (m^{-3}) is the normalized CCN concentration and k is a constant. Whenever CCN are depleted by activation as cloud droplets, an adverted scalar, $n_{\mathrm{CCN},a}$ (kg^{-1}), for the number mixing ratio of missing CCN that have already been activated is incremented. Nucleation is only possible if $s < s_{\mathrm{cut}}$. Here, C/ρ_a is a scalar advected within cloud and is reset to the environmental value, $C_{\mathrm{env}}(z)/\rho_a$, at all levels outside cloud. Initially, C/ρ_a is everywhere set equal to $C_{\mathrm{env}}(z)/\rho_a$, since there is no cloud yet.

TABLE 1. Microphysical conversion tendencies for mass mixing ratio (kg kg^{-1} s^{-1}). The final species in each interaction is the first symbol within parentheses, while symbols after the semicolon denote the initial interacting species. Corresponding symbols for tendencies of number mixing ratio (kg^{-1} s^{-1}) are denoted in a similar fashion, except with all hydrometeor quantities within the brackets being number (instead of mass) mixing ratios (kg^{-1}). Tendencies of droplet and crystal number from evaporation and sublimation are denoted by Ev(q_v; n_w) and Su(q_v; n_i). The origin of formulas in the present paper is also indicated, except for expressions taken from Lin et al. (1983, hereafter LF083) and Ferrier (1994, hereafter F94).

Symbol	Meaning	Origin
Ac(q_g; q_w|q_g)	Riming of cloud liquid by graupel	Section 2g
Ac(q_g; q_i|q_g)	Accretion of cloud ice by graupel	F94
Ac(q_g; q_s|q_g)	Accretion of snow by graupel	LFO83
Ac(q_g; q_r|q_g)	Accretion of rain by graupel	LFO83
Ac(q_g; q_r|q_i)	Accretion of cloud ice by rain	LFO83/F94
Ac(q_g/q_s; q_s|q_r)	Accretion of snow by rain, forming graupel or snow	LFO83
Ac(q_g/q_s; q_r|q_s)	Accretion of rain by snow, forming graupel or snow	LFO83
Ac(q_r; q_w|q_r)	Accretion of cloud liquid by rain	Section 2g
Ac(q_s; q_w|q_s)	Riming of cloud liquid by snow	Section 2g
Ac(q_s; q_i|q_s)	Accretion of cloud ice by snow	F94
Ac(q_s; q_w|q_i)	Snow from cloud ice by riming	LFO83
Au(q_r; q_w|q_w)	Autoconversion of cloud liquid to rain	Section 2g
Au(q_s; q_i|q_i)	Autoconversion of cloud ice to snow	Section 2g
Au(q_g; q_s|q_s)	Conversion of snow to graupel	Section 2h
Co(q_w; q_v|CCN)	Nucleation of droplets	Section 2e
Co(q_w; q_v)	Condensation onto (evaporation from) cloud liquid	Section 2e
Co(q_r; q_v)	Condensation onto (evaporation from) rain	Section 2e
De(q_i; q_v|IN)	Nucleation from deposition freezing	Section 2f
De(q_i; q_v)	Vapor deposition onto (sublimation from) cloud ice	Section 2e
De(q_s; q_v)	Vapor deposition onto (sublimation from) snow	Section 2e
De(q_g; q_v)	Vapor deposition onto (sublimation from) graupel	Section 2e
Ev$_{hom}$(q_v; q_w)	Evaporation during homogeneous freezing	Section 2f
Fr(q_i; CCN)	Nucleation from homogeneous freezing of CCN	Section 2f
Fr(q_i; q_w)	Nucleation from homogeneous droplet freezing	Section 2f
Fr(q_i; q_w|IN)	Nucleation from condensation freezing	Section 2f
Fr(q_i; q_w|CIN)	Nucleation from contact freezing	Section 2f
HM(q_i; q_w|q_s)	Rime-splintering of snow	Section 2f
HM(q_i; q_w|q_g)	Rime-splintering of graupel	Section 2f
Me(q_r; q_s)	Melting of snow to form rain	LFO83
Me(q_r; q_g)	Melting of graupel to form rain	LFO83
Me(q_w; q_i)	Melting of cloud ice	LFO83

For IN, the empirical activity spectrum observed by Meyers et al. (1992) is applied at temperatures between −5° and −30°C:

$$N_{\rm IN}\,({\rm m}^{-3}) = 1000\exp[12.96(S_i - 1) - 0.639] \times \Psi. \quad (11)$$

Here, Ψ is an empirical correction factor to account for the fact that the continental boundary layer, where the data for the empirical formula from Meyers et al. was obtained, is typically much richer in IN than the interior of the troposphere, especially at locations remote from land sources. Also, S_i is the saturation ratio with respect to ice. At colder temperatures between −30° and −80°C, a line of best fit to experimental data from a field campaign by DeMott et al. (2003) is applied:

$$N_{\rm IN}\,({\rm m}^{-3}) = 1000\{\exp[12.96(S_i - 1.1)]\}^{0.3}. \quad (12)$$

These data were obtained by sampling air from the free troposphere with a continuous-flow diffusion chamber (CFDC) at the top of Mount Werner in Colorado, and then separating the heterogeneous and homogeneous contributions to the crystal concentration. The correction factor, Ψ, is assigned a value of 0.06, in view of the need to match Eqs. (11) and (12) at −30°C and water saturation to avoid a discontinuity in heterogeneous nucleation there.

Whenever IN are depleted by activation as crystals, an advected scalar, $n_{{\rm IN},a}$ (kg^{-1}), for the number mixing ratio of IN lost due to nucleation is incremented. The quantities, $n_{{\rm CCN},a}$, $n_{{\rm IN},a}$, and C/ρ_a, are all advected and diffused like other scalars and are assumed to have zero terminal velocity. In the cloud-free environment, the values of $n_{\rm CCN}$, $_a$ and $n_{{\rm IN},a}$ are set to zero, since it is beyond the scope of this paper to quantify the large-scale advection of unactivated aerosol into the domain.

d. Terminal velocity

Sedimentation of cloud liquid and cloud ice is represented with formulas of the form, $v_x = \gamma a_x D_x^{b_x}$, where v_x (m s^{-1}) is the terminal velocity, $\gamma = \{[\rho_a(z = 0)/\rho_a(z)]\}^{1/2}$, while a_x and b_x are constants. For droplets, $a_w = 2.975 \times 10^7$ m$^{1-b_w}$ s^{-1} and $b_w = 2$ (Rogers and Yau 1991). Crystals are assumed to be columnar for the purposes of calculating the terminal velocity, since the majority of cirrus particles seen in the 2D-C probe data during CEPEX were columns or bullets (McFarquhar et al. 1999). Combining the mass–fall speed relation for hollow columns from laboratory studies by Kajikawa (1976), with an assumed bulk density for cloud ice, $\rho_i = 900$ kg m^{-3}, yields

$$a_i\,(\mathrm{m}^{1-b_i}\,\mathrm{s}^{-1}) = \frac{\rho_a(z = 1024\ \mathrm{m})}{\rho_a(z = 0)}\,2.53\left(\rho_i\,\frac{\pi}{6} \times 10^6\right)^{0.271}, \tag{13}$$

where $b_i = 0.813$. These columns (crystal type C1f) at sizes less than about 100 μm have a bulk density close to that of pure ice (e.g., Pruppacher and Klett 1997, 51–52; Kajikawa 1976), which is consistent with aircraft observations from CEPEX and CRYSTAL-FACE (section 2a). The vertical flux convergence terms in the evolution equations of mass and number mixing ratio, to account for the falling of a species of cloud particle, involve the mass- and number-weighted averages of v_x, respectively, over the local size distribution (Ferrier 1994).

e. Droplet nucleation

Cloud liquid mass is produced by nucleation followed by condensational growth. The activation step by which CCN are converted to droplets depends directly only on the supersaturation (see section 2c).

Activation only occurs when the supersaturation resolved on the model grid is positive. If this is true in cloud-free air, primary nucleation of droplets occurs, forming a cloud base. The peak supersaturation, $s_{v,w,\max}$ at cloud base is diagnosed analytically (Twomey 1959; Cohard and Pinty 2000). In real clouds, this peak in supersaturation is located only very close to (typically about 10 m above) the cloud base itself and cannot be resolved by the predicted vapor mixing ratio on the model grid.

Elsewhere within the cloud, in-cloud (or secondary) droplet nucleation may occur. If the number concentration and volume-mean size of droplets is typical for clouds and fogs ($\sim$1 cm^{-3} or more, 1 μm or more; Pruppacher and Klett 1997) then a grid point is assumed to be in cloud. The supersaturation resolved on the model grid, $\bar{s}$, is then applied for droplet nucleation. A linearized solution of the evolution equations for vapor mixing ratio and temperature during the time step (see appendix) is utilized to predict $\bar{s}$, and the mass of vapor condensed or deposited onto hydrometeors [Co(q_y; q_v) for $y = w, r$ or De(q_x, q_v) for $x = i, s, g$]. The justification for applying the resolved supersaturation to in-cloud droplet nucleation is that the supersaturation tends to vary quite smoothly with height, well above the peak at cloud base (Rogers and Yau 1991).

Activation only occurs if $s > 0.01\%$ (s is either $s_{v,w,\max}$ $\bar{s}$, near the cloud base or in-cloud, respectively), a minimum value derived from the observed range of supersaturations seen in fogs (Pruppacher and Klett 1997);

$$\mathrm{Co}(n_w; q_v|\mathrm{CCN})(0.01\% < s < s_{\mathrm{cut}}) = \frac{\max[Cs^k - n_{\mathrm{CCN},a}\rho_a, 0]}{\Delta t \rho_a}. \tag{14}$$

Here, Co(n_w; q_v|CCN) is the increment to the number mixing ratio of droplets generated in time step Δt (s). When $s > s_{\mathrm{cut}}$, the supersaturation determining Co(n_w; q_v|CCN) is replaced by s_{cut}. The diameter of newly nucleated droplets, D_{crit}, is given by Cohard and Pinty (2000), and determines the corresponding increment of cloud liquid mass, Co(q_w; q_v|CCN). Also, $n_{\mathrm{CCN},a}$ is incremented by Co(n_w; q_v|CCN)/p_a whenever CCN are lost by activation.

In the manner of Cohard and Pinty (2000) and Khairoutdinov and Kogan (2000), the number of droplets is not changed by partial evaporation. An exception to this occurs if the mean droplet size becomes very low ($<$10 μm), with the droplet number then being reduced by the same fraction as the cloud liquid mass [Ev(q_v; n_w)]. Sublimation of cloud ice is treated similarly [Su(q_v; n_i)].

f. Ice nucleation

For primary ice nucleation, the formula of condensation and deposition freezing from Meyers et al. (1992) is applied between $-5°$ and $-30°$C, with a line of best fit from aircraft data (DeMott et al. 2003) being used for temperatures between $-30°$ and $-80°$C (see section 2c):

$$\mathrm{De}(n_i; q_v|\mathrm{IN}) + \mathrm{Fr}(n_i; n_w|\mathrm{IN}) = \frac{\max(N_{\mathrm{IN}} - n_{\mathrm{IN},a}\rho_a, 0)}{\Delta t \rho_a}. \tag{15}$$

Newly nucleated crystals are assumed to start as pure ice spheres with a diameter of 10 μm. Naturally, $n_{\mathrm{IN},a}$ is then incremented by [De(n_i; q_v|IN) + Fr(n_i; n_w|IN)]/ρ_a.

When there is ample cloud liquid, $\mathrm{De}(n_i; q_v|\mathrm{IN}) = 0$ and the mass of nucleated crystals is deducted from the cloud liquid [$\mathrm{Fr}(q_i; q_w|\mathrm{IN})$]; otherwise, the mass of newly nucleated crystals is deducted from the vapor by deposition freezing and $\mathrm{De}(q_i; q_v|\mathrm{IN}) > 0$.

Contact nucleation is represented in the manner of Young (1974), Cotton et al. (1986), Pruppacher and Klett (1997), and Ovtchinnikov et al. (2000), with sources of number due to the forces of Brownian motion, thermophoresis, and diffusiophoresis acting on the CIN aerosol. An active CIN can only form an ice particle if these forces cause it to collide with a supercooled droplet. A temporary grid of size bins is created to represent the predicted size distribution of cloud droplets. Contact nucleation is performed separately for each bin. The formula for N_{cn}, the number concentration of active CIN, is from Meyers et al. (1992), being modified here by the same factor Ψ as in Eq. (11). This factor Ψ accounts for the relative scarcity of insoluble aerosol aloft at midtropospheric levels compared to the surface where the measurements utilized by Meyers et al. were made. No separate prognostic variable for the number of CIN activated is incremented when contact nucleation occurs (e.g., Carstens and Martin 1982; Baker 1991; Ovtchinnikov et al. 2000). It is assumed that the CIN are clay aerosol particles with an average radius of 0.3 μm (Ovtchinnikov et al. 2000).

Secondary production of ice occurs by the Hallett–Mossop (HM) process of ice multiplication (Hallett and Mossop 1974) between $-3°$ and $-8°$C and involves 350 ice splinters emitted for every milligram of liquid at $-5.5°$C rimed onto snow or graupel [$\mathrm{HM}(n_i; n_w|q_s)$ and $\mathrm{HM}(n_i; n_w|q_g)$] (e.g., Swann 1998a). The HM splinters are assumed to start as spheres of pure ice 5 μm in diameter [$\mathrm{HM}(q_i; q_w|q_s)$ and $\mathrm{HM}(q_i; q_w|q_g)$].

Homogeneous aerosol freezing is assumed to occur instantaneously when a size- and temperature-dependent critical supersaturation with respect to ice is exceeded. It is represented by generating a temporary grid of mass-doubling bins for the predicted size distribution of unactivated aerosols. A lookup table for the critical saturation ratio at which CCN freeze homogeneously is based on the theory proposed by Koop et al. (2000). After homogeneous aerosol freezing, $n_{\mathrm{CCN},a}$ is updated and the corresponding tendency of crystal number is stored in $\mathrm{Fr}(n_i; q_v|\mathrm{CCN})$. Since the aerosol composition aloft is assumed to be ammonium sulfate, there is an option for a correction of -30% to be applied to all values of $S_{i,\mathrm{crit},j}$ to account for the deviation from theory that has been observed in laboratory experiments with the Aerosol Interactions and Dynamics in the Atmosphere (AIDA) cloud chamber by Mangold et al. (2005). Aircraft CFDC data analyzed by DeMott et al. (2003) and most laboratory experiments (Bertram et al. 2000; Prenni et al. 2001; Hung et al. 2002) have not shown any deviation from the theory of Koop et al., however.

Homogeneous droplet freezing is performed by instantaneous conversion of a fraction of the supercooled cloud liquid to cloud ice at temperatures colder than $-36°$C. Virtually all homogeneous freezing of cloud liquid occurs in a layer between about $-35°$ and $-37°$C that is about 200 m deep (Heymsfield et al. 2005). The larger droplets in the droplet size distribution freeze first and their vapor growth can cause total evaporation of the smaller supercooled droplets. Heymsfield et al. (2005) found that the fraction of small droplets disappearing by evaporation is higher at lower vertical velocities. Typical vertical resolutions of CSRMs cannot resolve the decline of supersaturation with increasing altitude within this layer, which is caused by the vapor growth of new frozen droplets. They cannot resolve the precise temperature at which exact water saturation is reached, which determines the fraction of droplets to be evaporated. So, a parameterization of the evaporation of small droplets during homogeneous freezing is needed, irrespective of the time step. In the present study, the fraction by number of cloud droplets that are frozen homogeneously just above the $-36°$C level is parameterized with a 3D lookup table as a function of the vertical velocity (w), the predicted supersaturation at the level just below the homogeneous freezing, s^* (normalized by the product of n_w/w and $\langle D_w \rangle$), and the product of n_w and $\langle D_w \rangle$. Here, $\langle\rangle$ denotes a number-weighted average over the particle size distribution. Data for the freezing fraction are obtained from a spectral microphysics parcel model, which is a simplified version of the model of Phillips et al. (2005). It is run over a wide range of aerosol concentrations ($50 < C < 50\,000$ cm^{-3}) and vertical velocities ($0.3 < w < 50$ m s^{-1}). The freezing fraction determines $\mathrm{Fr}(n_i; n_w)$. The remaining droplets are evaporated [$\mathrm{Ev}_{\mathrm{hom}}(q_v; q_w)$].

The justification for the choice of these three input variables for the lookup table is that the fraction of droplets to be evaporated must be governed by the distance ascended until the supersaturation reaches zero, which is related to 1) the source of supersaturation from ascent (linked to w); 2) the initial supersaturation when freezing commences; and 3) the sink of supersaturation from vapor deposition onto frozen droplets (related to the first moment of their size distribution). Homogeneous freezing of droplets is assumed to occur instantaneously at a size-dependent critical temperature (Pruppacher and Klett 1997) in the

parcel model, in view of the rapidity of freezing of a given droplet. The droplet size distribution in the parcel model is fitted to a gamma distribution ($p_w = 3.5$) of the form applied in the present CSRM simulations just before freezing begins. Finally, all rain is frozen homogeneously at −35°C.

g. Autoconversion of cloud to precipitation

Autoconversion of droplets to rain is performed in the manner presented by Lin et al. (1983), except that the threshold on the cloud-liquid mixing ratio is replaced by the product of the predicted droplet number mixing ratio and the mass of a droplet of a critical size, $D_{w,\text{auto}}$ (about 20 μm). The justification for this is that autoconversion displays a threshold behavior with respect to average droplet size (e.g., Khairoutdinov and Kogan 2000; Pawlowska and Brenguier 2000; Tripoli and Cotton 1980). The relative dispersion implied by the choice of p_w and the predicted droplet number replace the values prescribed by Lin et al. in the autoconversion rate [$\text{Au}(q_r; q_w|q_w)$]. Autoconversion of crystals to snow [$\text{Au}(q_s; q_i|q_i)$] is performed when the average size of crystals exceeds a critical threshold, $D_i = 200$ μm, in the manner presented by Ferrier (1994).

h. Accretion of cloud by precipitation

The preferential accretion of large droplets has a major impact on the mean droplet size (e.g., Phillips et al. 2005). Hence, when evaluating rates of accretion of cloud by precipitation [$\text{Ac}(q_y; q_x|q_y)$ and $\text{Ac}(n_y; n_x|n_y)$, where $y = r, s, g$ and $x = w, i$], the approximation is made that cloud particles smaller and larger than a critical size have collision efficiencies of zero and unity, respectively. This critical size is $D_{w,\text{crit}} = 15$ μm for droplets and $D_{i,\text{crit}} = 40$ μm for crystals (Rogers and Yau 1991, see their Fig. 8.3; Ferrier 1994).

Conversion of snow to graupel as originally formulated by Lin et al. (1983) was independent of riming rate. This was unphysical since graupel is, by definition, highly rimed. Consequently, a version of the semiempirical parameterization innovated by Swann (1998a) is implemented instead. If the snow content exceeds about 0.5 g m^{-3} and $\text{Ac}(q_s; q_w|q_s) > 0$, then

$$\text{Au}(q_g; q_s|q_s) = 0.5 \max\{\text{Ac}(q_s; q_w|q_s) - [\text{Ac}(q_s; q_i|q_s) + \text{De}(q_s; q_v)], 0\}. \quad (16)$$

As with Lin et al., accretion of cloud ice by supercooled rain can yield graupel.

3. Description of numerical model and experimental design

a. CSRM

The CSRM utilized in the present study is the Weather, Research, and Forecasting (WRF) model described by Phillips and Donner (2007). The Geophysical Fluid Dynamics Laboratory (GFDL) radiation code (Freidenreich and Ramaswamy 1999; Schwarzkopf and Ramaswamy 1999) has been incorporated into this version of WRF, including representations of the shortwave and longwave single-scattering properties for cloud liquid (Slingo 1989; Held et al. 1993), cloud ice (Fu 1996; Fu et al. 1998), rain, and snow (Savijarvi 1997; Fu et al. 1995). These representations include dependences on predicted sizes of hydrometeors, such as particles of cloud liquid and cloud ice. For the single-scattering properties of cloud ice, a generalized effective size is inferred from the mean (represented by angle brackets) size of the equivalent spherical diameter, $\langle D_i \rangle = (1 + p_i)/\lambda_i$, with a lookup table for $D_{\text{ge},i}/\langle D_i \rangle$ (where $D_{\text{ge},i}$ is the generalized effective size). This lookup table was generated by integrating numerically the formula for the generalized effective size of cloud ice given by Fu (1996) for a range of values of $\langle D_i \rangle$. Crystals are assumed to be columnar (McFarquhar et al. 1999) with a ratio of length to width, L/D, specified from aircraft observations (Ono 1969; Auer and Veal 1970) in the manner of Fu and Liou (1993), obeying a gamma size distribution ($p_i = 1$). This axial ratio varies between 1 and almost 5 for $D = 20$–160 μm. For single-scattering properties of cloud liquid, the effective diameter is $D_{e,w} = (3 + p_w)/\lambda_w$.

b. Experimental design

Two cases have been selected for simulations with the double-moment bulk microphysics scheme implemented in WRF. These are TOGA COARE (20–25 December 1992), a case of vigorous deep convection with maximum cloud-top levels of about 12–14 km MSL, and KWAJEX (17–31 August 1999) in which convection was weaker with cloud tops usually below 10 km MSL. These cases were selected because observed tendencies representing the domain-averaged advection are available for them. In view of the lack of microphysical observations from aircraft during the TOGA COARE case at subzero levels, the WRF simulations of TOGA COARE are compared with observational data from CEPEX.

For simulations of TOGA COARE and KWAJEX presented here, WRF is integrated with a 2-km horizontal resolution and a 500-m vertical resolution. The

vertical grid has 40 levels. A time step of 10 s is used. The horizontal domain size in 2D is 170 km long. Observed profiles of temperature and moisture, and corresponding tendencies representing the domain-averaged advection, are from Ciesielski et al. (1997) for TOGA COARE. For KWAJEX, Dr. M. Zhang of Stony Brook University has generated the tendencies for domain-averaged advection with the multivariate constrained optimization method of Zhang et al. (2001). Observed time series of sea surface temperature (SST) were applied in both cases. Perturbations on the initial field of vapor mixing ratio were imposed so as to initiate convection, as done by Donner et al. (1999) and Lipps and Hemler (1986). These perturbations are vertically uniform and horizontally random within the range ± 2 g kg^{-1}. Lateral boundary conditions are periodic for all prognostic variables. Other aspects of the model setup are as described by Donner et al. (1999) and Phillips and Donner (2007).

Figure 1 displays the vertical profiles of normalized environmental concentration of CCN, C, prescribed for WRF simulations of TOGA COARE and KWAJEX. The profiles are obtained mostly by combining aircraft observations from several field experiments in tropical oceanic regions. The condensation nuclei (CN) concentration measured on the Electra aircraft for 10 days during December 1992 of TOGA COARE (http://dss.ucar.edu/datasets/ds606.1) has a geometric mean of almost 500 cm^{-3} at levels in, and just above, the boundary layer outside cloudy regions. Assuming that half of all CN are activated at a supersaturation of 1% and that $k = 0.5$ (Pruppacher and Klett 1997), $C = 250$ cm^{-3} for the boundary layer with all activation ceasing at $s_{\text{cut}} = 2^{1/k} = 4\%$. In the free troposphere, the vertical profile of C is prescribed from aircraft observations in the Global Backscatter Experiment (GLOBE-2; Clarke and Kapustin 2002) at 10–14 km MSL near the intertropical convergence zone (ITCZ) and from CRYSTAL-FACE (Phillips et al. 2005) above 14 km MSL. The aerosol profile for KWAJEX is prescribed from a global model near the sea surface (Spracklen et al. 2005), and from aircraft observations in GLOBE-2 near Honolulu (Clarke 1993) and in the Pacific Exploratory Missions Tropics (PEMT-B) experiment (Clarke and Kapustin 2002) at 10–14 km MSL. The chemical composition of the aerosol at all levels is assumed to be ammonium sulfate (Pruppacher and Klett 1997; Spracklen et al. 2005). A vertical profile of environmental concentration of IN for condensation/deposition freezing is also displayed in Fig. 1, being based on aircraft observations by DeMott et al. (2003) and a modified version of the formula from Meyers et al. (1992) (see section 2c).

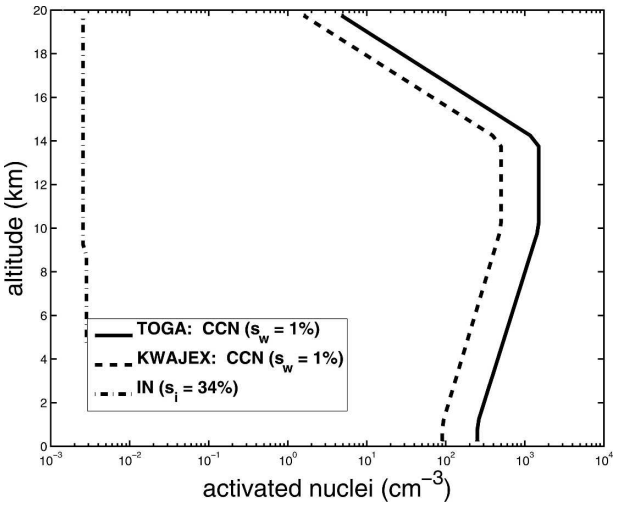

FIG. 1. Environmental concentrations of CCN and IN (cm^{-3}), providing inputs for the TOGA COARE and KWAJEX simulations.

4. Results from CSRM simulations and comparison with observations

Evaluation of WRF simulations, for TOGA COARE (the TOGA control) and KWAJEX (the KWAJEX control; section 3), relies on aircraft data from the CEPEX (4 April 1993; McFarquhar et al. 1999) and KWAJEX (Heymsfield et al. 2002) field campaigns, respectively, above the freezing level. There are virtually no data from the Electra aircraft during TOGA COARE at subzero levels. Profiles of particles presented here are conditionally averaged at each level over regions where the cloud is predicted to be visible (an optical depth >0.2 over a 500-m layer) and highly visible (an optical depth >3 over a 500-m layer) for comparison with CEPEX and KWAJEX aircraft data respectively. The sampling criteria differ between both cases, because aircraft sampled visible cloud during CEPEX but only cloud decks (typically about 4 km deep) with a total optical depth of at least about 23 in KWAJEX (Heymsfield et al. 2002). Exact agreement between model simulations of TOGA COARE (equatorial western Pacific Ocean; °2°S, 156°E; December 1992) and CEPEX (equatorial central Pacific Ocean; °15°S, 179°E; April 1993) observations is not to be expected in view of the fact that the intensity of the deep convection, the cloud-top heights and the environmental CCN concentration must have been different. Also, the deep convection observed in KWAJEX was mostly shallower than in TOGA COARE, with cloud tops in the range of 8–11 km MSL (about $-20°$ to $-50°$C; Heymsfield et al. 2002). KWAJEX was in a more remote part of the Pacific (tropical western Pacific Ocean;

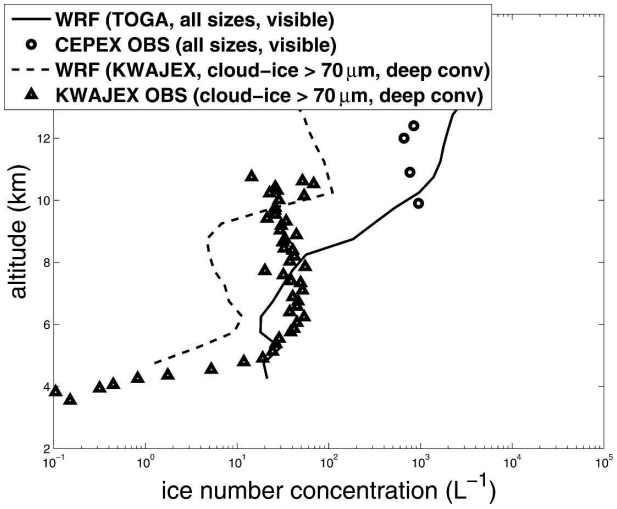

FIG. 2. Number concentration for cloud ice particles predicted in the TOGA COARE and KWAJEX simulation, compared with aircraft observations from CEPEX (McFarquhar et al. 1999) for 4 Apr 1993 and from KWAJEX. The observed and predicted 2-DC concentrations of crystals (>70 μm) in KWAJEX are also shown (Heymsfield et al. 2002). Predicted profiles are conditionally averaged over all data points with optical depths, τ, exceeding 0.2 (visible) and 3 (deep conv) for TOGA COARE and KWAJEX simulations, respectively, at each vertical level.

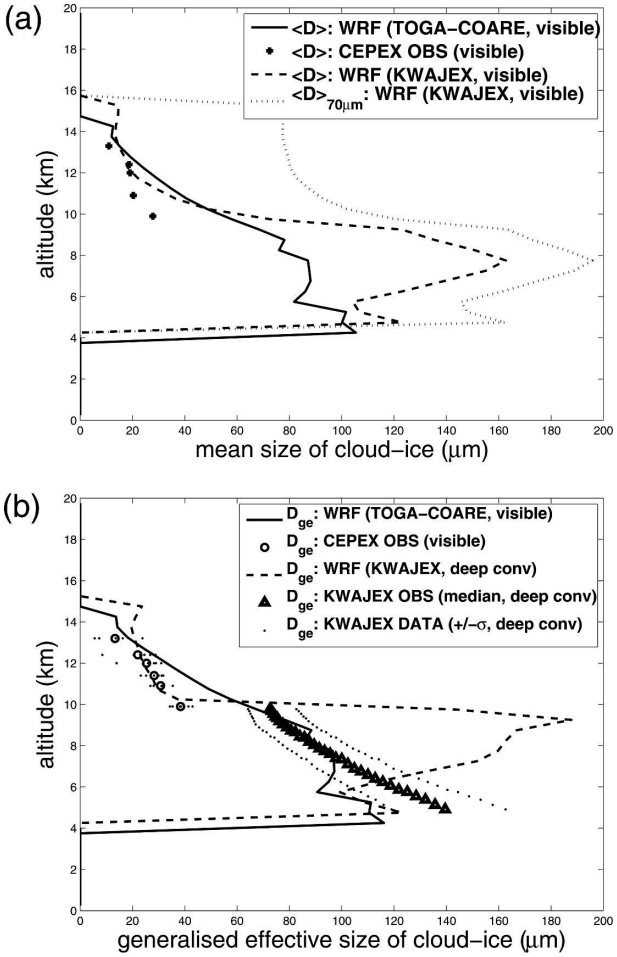

FIG. 3. (a) Mean size $\langle D_i \rangle$ and (b) generalized effective size $D_{\mathrm{ge},i}$ for cloud ice predicted in the TOGA COARE and KWAJEX simulations, compared with CEPEX and KWAJEX aircraft observations. Also shown is the (number-weighted) mean size of cloud ice particles >70 μm for the TOGA COARE simulation in (a). Model data are averaged in the same manner as for Fig. 2.

9°N, 167°E; August 1999) where the CCN concentration is lower, compared to TOGA COARE.

Figure 2 shows the number concentration of cloud-ice particles observed with the 2D-C probes for all flight days in KWAJEX, compared with that predicted in the KWAJEX control. The 2D-C ice concentration includes only particles larger than about 70 μm. The altitude of the peak in this ice concentration agrees well between the model and the KWAJEX observations: about 6 km MSL, which is near the top of the HM generation region. In the model, this peak is caused by generation of HM splinters by ice particle multiplication. However, the predicted 2D-C ice concentration of this peak is about half an order of magnitude too low compared to observations. The HM process is a process of multiplication and is inherently difficult to simulate. Also shown in Fig. 2 is the total ice particle concentration inferred from aircraft data in CEPEX and predicted in the TOGA control. The observed ice concentration is about 50% lower than that predicted by WRF at most observational levels, as expected from the lower concentration of CN in CEPEX compared to TOGA COARE (Spracklen et al. 2005; Clarke and Kapustin 2002).

Figure 3 shows profiles of mean size, $\langle D_i \rangle$, and generalized effective size, $D_{\mathrm{ge},i}$ (Fu 1996), of cloud-ice particles from the model in comparison with aircraft data from CEPEX and KWAJEX. Above 12 km MSL, there is good agreement in $\langle D_i \rangle$ and $D_{\mathrm{ge},i}$ between the TOGA control and CEPEX observations, in view of the spread of individual data points around their mean values. A high bias of about 10 μm is evident below this level. Also shown in Fig. 3 are profiles for KWAJEX of $D_{\mathrm{ge},i}$ for all days of aircraft observations (Heymsfield et al. 2002) based on measurements of crystals >70 μm and from the KWAJEX control. The increase of $\langle D_i, \rangle$ when crystals <70 μm are omitted from the averaging suggests that the generalized effective size predicted by WRF would probably be increased similarly by omitting these small crystals, which would imply a high bias in $D_{\mathrm{ge},\,i}$ of between 10% and 100% varying with altitude relative to KWAJEX observations. There are at

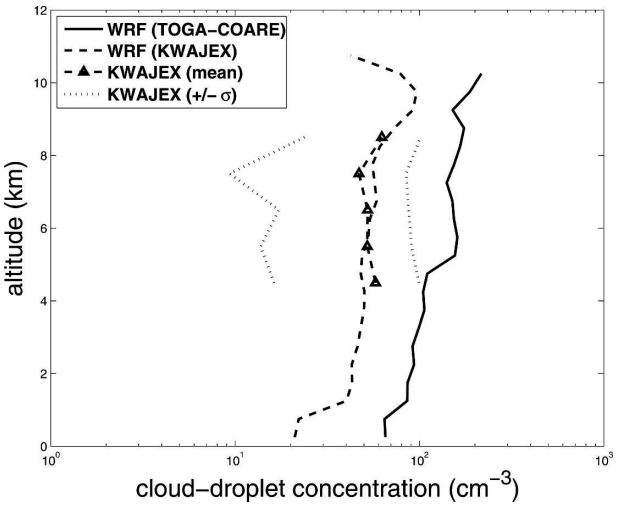

FIG. 4. Number concentration of cloud droplets predicted in the TOGA COARE and KWAJEX simulations, compared with KWAJEX aircraft observations. Model data are conditionally averaged over data points where $\tau > 0.2$ and $\tau > 3$ at each level in TOGA COARE and KWAJEX, respectively.

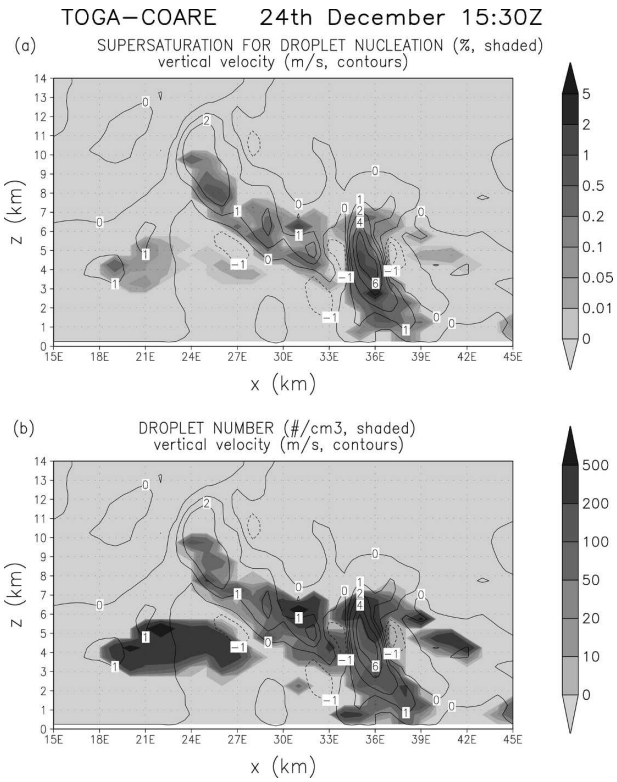

FIG. 5. (a) Supersaturation (%) and (b) droplet number concentration in a snapshot of a storm on 24 Dec 1992 from a WRF simulation of TOGA COARE.

least two possible reasons for such a bias. First, the empirical dependence of p_i on λ_i has not yet been included in the model. Second, there are too few crystals at these levels as noted above, and the competition for available vapor is too weak during vapor growth.

Figure 4 depicts mean number concentrations of cloud droplets from WRF and from aircraft observations for all flights in KWAJEX (no FSSP data are available for 22 August 1999). The predicted droplet concentration for the KWAJEX control has an error of about 10% or less compared with KWAJEX observed values at all levels where a comparison is possible. The predicted droplet concentration in the TOGA control is higher by about 100% at all observational levels relative to KWAJEX values, as expected from the higher CN concentration in TOGA COARE compared to KWAJEX (Spracklen et al. 2005).

Figure 5 shows a snapshot of the predicted supersaturation with respect to water in a deep convective updraft and the coincident droplet number concentration in the TOGA COARE simulation. As expected (e.g., Rogers and Yau 1991) at levels where liquid is present (i.e., below 10 km MSL), the supersaturation is positive in regions of ascent and negative otherwise. Note the discontinuity in supersaturation just above 10 km MSL where homogeneous freezing of supercooled liquid occurs at −36°C, as seen in aircraft observations (Heymsfield et al. 2005).

Figure 6 shows two histograms of relative frequency, f, of in-cloud supersaturation with respect to water and vertical velocity from cloudy points with a combined cloud liquid and cloud ice mixing ratio >0.001 g kg^{-1} in the TOGA control. The data points have been grouped into 21 size bins (logarithmically spaced) and 21 supersaturation bins (equally spaced) over the plotted domain. In the histogram at subzero temperatures (−32° to −36°C), vapor growth of ice contributes to conditions subsaturated with respect to water at vertical velocities less than about 1–2 m s^{-1}. The other histogram at warmer temperatures shows an increase in supersaturation with vertical velocity above about 1 m s^{-1}, with supersaturations being mostly positive throughout the entire range of vertical velocities. Figure 6c, which shows $s_{v,w,\max}(w)$, demonstrates that in-cloud droplet nucleation is to be expected in deep convective updrafts because this peak supersaturation at cloud base will frequently be exceeded by the in-cloud supersaturation shown in the histograms.

Radiative fluxes are compared in Table 2 between observations from TOGA COARE, and the TOGA control. One set of observed fluxes was obtained from P. Minnis at NASA Langley (e.g., Minnis et al. 1995) for the top of the atmosphere and from Improved Me-

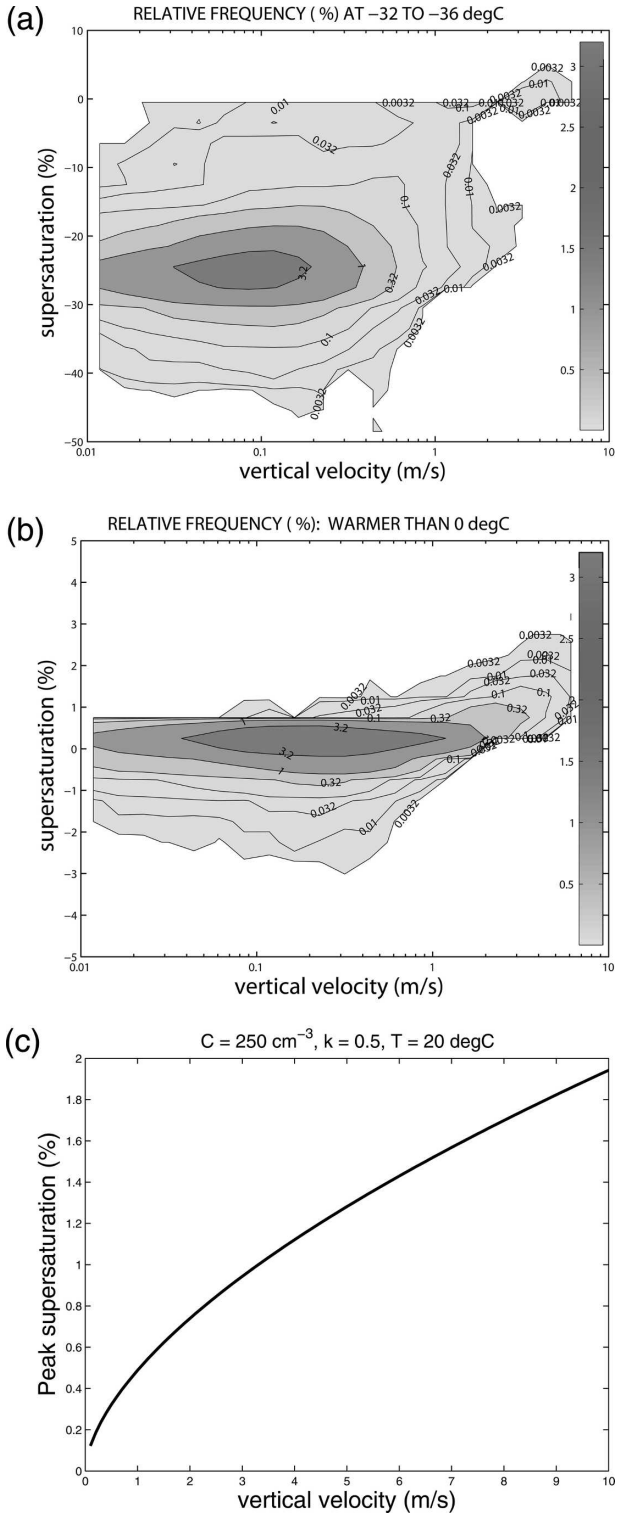

FIG. 6. Relative frequency (%) of supersaturation with respect to liquid at (a) −30° to −36°C and (b) temperatures warmer than 0°C, from the simulation of TOGA COARE. (c) The cloud-base supersaturation as a function of w at 20°C.

teorology (IMET) buoy data (Weller and Anderson 1996; Burks 1998) for the surface. Another set of fluxes from the International Satellite Cloud Climatology Project (ISCCP; Zhang et al. 1995; Rossow and Zhang 1995) was utilized. Errors in the predicted fluxes are all 2%, or less, at the top of the atmosphere (ISCCP) and the surface (IMET). This agreement is much better than was obtained with the single-moment scheme by Phillips and Donner (2007).

Figure 7 shows a plot of supercooled liquid water content in the −32° to −36°C layer, as a function of vertical velocity for cloudy points (as defined for Fig. 6). This layer is immediately below the level of homogeneous droplet freezing. The liquid water content is close to zero at vertical velocities <1–2 m s^{-1}, because of subsaturated conditions noted above. Consequently, homogeneous freezing of activated droplets is found to be mostly restricted to deep convective updrafts ≥2 m s^{-1}, as noted by Heymsfield et al. (2005).

Also shown in Fig. 7 is the relative frequency of supersaturation with respect to ice at levels between −40° and −80°C, evaluated as in Fig. 6. It again illustrates a threshold behavior over the range of vertical velocities. For $0.05 < w < 1$ m s^{-1}, the highest values of supersaturation are about 50%–60% but fall to less than 10% for all $w >$ 1–2 m s^{-1} and are less than 50% at $w <$ ~0.05 m s^{-1}. Supersaturations with respect to ice of about 50% or more are necessary for homogeneous aerosol freezing in the model at most levels above 11 km MSL (e.g., Koop et al. 2000). This suggests that homogeneous aerosol freezing in the TOGA control simulation is restricted to areas of weak ascent in a range of vertical velocities between ~0.05 and 1 m s^{-1}, being most likely at about 0.5 m s^{-1}. The reason is that homogeneous freezing of cloud liquid occurs exclusively in the deep convective updrafts ≥2 m s^{-1}, as noted above. In such rapid updrafts, the vapor growth of homogeneously frozen cloud droplets at high concentrations >1–10 cm^{-3} prevents the supersaturation with respect to ice from reaching the critical thresholds near 50% necessary for homogeneous aerosol freezing (Phillips et al. 2005). Also, if the ascent is too weak (e.g., <~0.05 m s^{-1}), then vapor growth of preexisting ice particles (e.g., from heterogeneous nucleation) prevents the supersaturation from reaching the critical values for homogeneous aerosol freezing. Furthermore, the number concentration of aerosols freezing homogeneously is diminished by the lower peak supersaturation at lower vertical velocities (Karcher and Lohmann 2002).

The total number of aerosols frozen homogeneously is almost 10 times that of homogeneously frozen drop-

TABLE 2. Longwave and shortwave fluxes at the top of the atmosphere (TOA) and the earth's surface (SFC). The initial 1.5 days of the 6-day simulated period were omitted from the time-averaging here, to allow time for the model to spin up after the onset of convection.

		Shortwave flux (W m^{-2})		Longwave flux (W m^{-2})	
Case	Simulation/observations	TOA upward	SFC downward	TOA upward	SFC downward
TOGA COARE	WRF	206.6 (1%)	112.7 (−2%)	169.2 (1%)	429.2 (0.3%)
	Observed (Minnis/IMET)	208.2	115.0	167.1	427.7
	Observed (ISCCP)	204.5	146.2	167.3	458.6

lets, when counted over the entire domain and duration of the TOGA control run. Their numbers are about 2 orders of magnitude higher than the corresponding total number of HM splinters, which in turn is 2 and 0.5 orders of magnitude higher than the total numbers of heterogeneous crystals nucleated in and above the mixed-phase region, respectively. In the KWAJEX control, total numbers of droplets and aerosols freezing homogeneously throughout the entire domain are comparable. The absence of upper-level cirrus aloft observed during most of the KWAJEX flights (Heymsfield et al. 2002) is consistent with a lack of homogeneous ice in the KWAJEX control.

5. Roles of nucleation processes in TOGA COARE

Results from sensitivity tests are presented to establish the relative roles of nucleation processes in the TOGA COARE simulation (the TOGA control). As in section 4, vertical profiles presented here are conditional averages at each level over regions where the cloud is predicted to be visible.

a. Homogeneous ice nucleation

Four simulations were performed with exclusion from the TOGA control run of homogeneous freezing of aerosols (the no-homogeneous aerosol freezing/TOGA case), cloud droplets (the no-homogeneous droplet freezing/TOGA case), and all particles (the no-homogeneous freezing/TOGA case). Also a run without preferential evaporation of small droplets during their homogeneous freezing (the no-droplet evaporation/TOGA case) was performed.

Figure 8 shows that by far the most dramatic alteration occurs when homogeneous freezing of both cloud droplets and aerosols is excluded. The average concentration of ice particles is reduced by 2–3 orders of magnitude in the no-homogeneous freezing/TOGA case at levels above 10–11 km MSL (about −40°C) and by more than an order of magnitude in most of the mixed-phase region (about 5–10 km MSL; 0° to −36°C), relative to the TOGA control. Consequently, the descent of homogeneously frozen aerosols and droplets (e.g., by sedimentation) has a crucial impact on the domainwide concentration of cloud ice in the mixed-phase region in

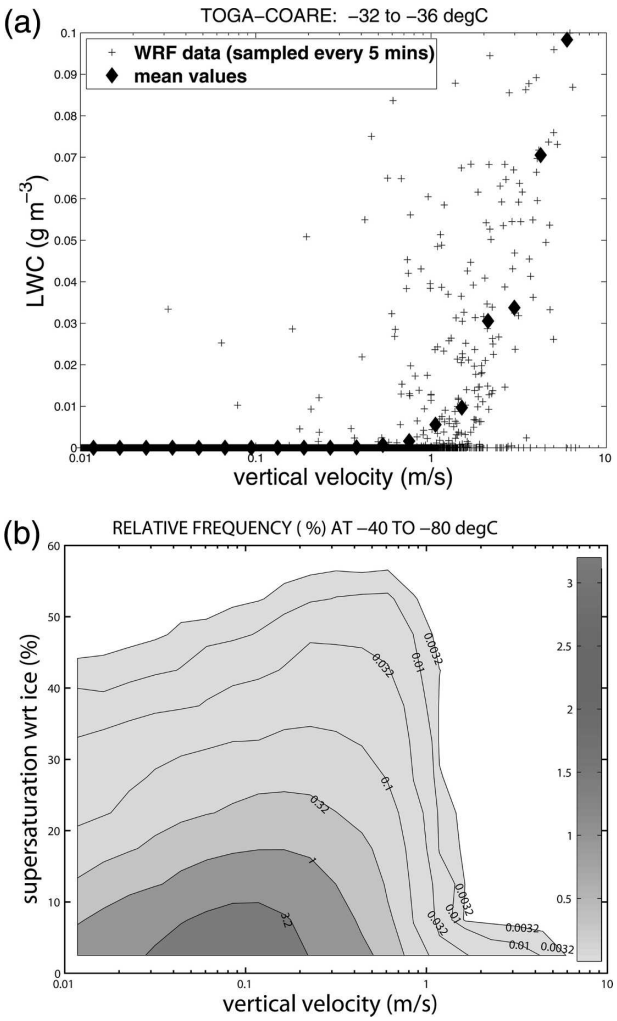

FIG. 7. (a) Supercooled cloud liquid (−32° to −36°C), as a function of vertical air velocity, subsampled at a frequency of 5 min, and (b) relative frequency (%) of positive supersaturation with respect to ice (−40° to −80°C), from the simulation of TOGA COARE.

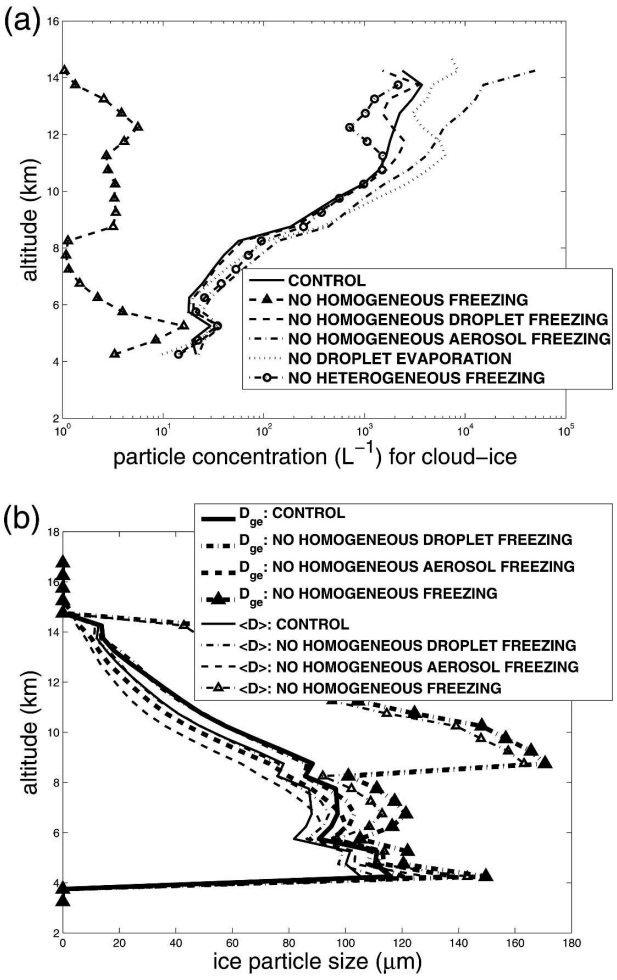

FIG. 8. (a) Number concentration and (b) size of cloud ice particles from the TOGA control and from corresponding simulations without homogeneous freezing of aerosols, droplets, and all liquid particles (aerosols, droplets, and rain) and without all heterogeneous freezing. Also shown is the ice concentration profile from the simulation without preferential evaporation of smaller droplets during homogeneous freezing. Model data are averaged in the same manner as for Fig. 2.

the TOGA control. However, at subzero levels just below about 6 km MSL (−7°C), the HM process produces most of the crystals and there is less sensitivity with respect to exclusion of all homogeneous freezing. The average sizes of ice particles are approximately doubled or tripled at most subzero levels in the no-homogeneous freezing/TOGA case relative to the TOGA control, because of the lower concentrations of heterogeneous, relative to homogeneous, ice, which reduces competition for vapor during diffusional growth.

Exclusion of homogeneous aerosol freezing is found to increase the average concentration of cloud ice by 0.5–1 orders of magnitude at all levels above 11 km MSL (−43°C). At these upper levels, there is nucleation of supercooled droplets that immediately freeze homogeneously at high concentrations. Prohibition of homogeneous freezing of cloud droplets slightly perturbs the cloud ice concentration by up to ±30% above 11 km MSL by altering homogeneous aerosol freezing, but the change below this level is negligible. Consequently, most crystals descending through the mixed-phase region are likely to be homogeneously frozen aerosols.

Preferential droplet evaporation, which has not been parameterized before in any bulk microphysics scheme, suppresses homogeneous droplet freezing appreciably in the TOGA control run. The ice concentration at 10–12 km MSL, near the level of homogeneous droplet freezing, is about half an order of magnitude higher in the no-droplet evaporation/TOGA case relative to the TOGA control. Throughout the mixed-phase region it is about 50%–100% higher. The total number of droplets frozen homogeneously throughout the entire domain is tripled by exclusion of this evaporation of droplets during homogeneous freezing.

Finally, there are perturbations by up to 5–10 μm in the average sizes of cloud ice particles at most subzero-levels in the no-homogeneous aerosol freezing, no-droplet evaporation, and no-homogeneous droplet freezing/TOGA cases relative to the TOGA control.

b. Heterogeneous nucleation of cloud ice

A run was performed without any heterogeneous nucleation (the no-heterogeneous freezing/TOGA case) and compared with the TOGA control. At most subzero levels in the mixed-phase region, the ice concentration is augmented by up to about 50% in the no-heterogeneous freezing/TOGA case relative to the TOGA control (Fig. 8). Above 11 km MSL (−43°C) it is reduced by a similar fraction. The comparative weakness of this response again points to the predominance of homogeneous freezing processes in the TOGA-control run. The reduction above 11 km MSL occurs because homogeneous aerosol freezing occurs at lower vertical velocities, yielding lower concentrations of crystals (e.g., Karcher and Lohmann 2002), in the no-heterogeneous freezing/TOGA case. Total numbers of homogeneously frozen droplets, summed over the whole domain, are also boosted (by about 20%) in the absence of heterogeneous ice.

The total number, summed over the entire domain, of primary crystals formed by contact nucleation is about 3 orders of magnitude less than for crystals nucleated by condensation and deposition freezing in the mixed-phase region of the TOGA control. Consequently, an extra run with exclusion of contact nucleation from the TOGA control produces little impact at

most subzero levels. This is partly because in any subsaturated cloudy regions, where thermophoresis actually favors contact nucleation, the cloud liquid tends to disappear quickly by evaporation before it can freeze.

c. Secondary ice production

A run was performed with the HM process of ice particle multiplication prohibited (the no-HM/TOGA case) from the TOGA control. When the HM process is excluded, the ice concentrations below 6 km MSL (−7°C) and at 12–14 km MSL (−51° to −67°C) are reduced by up to about a third of an order of magnitude. Also, HM splinter production acts to boost the numbers of aerosols that freeze homogeneously, for the same reason that heterogeneous freezing does, as noted above. The HM splinters are much more numerous than heterogeneous crystals (section 4). The mean and generalized effective sizes of cloud ice are augmented by up to about 50 μm in the HM region when the HM process is prohibited due to reduced competition for vapor during growth, with changes elsewhere being minimal.

d. All processes of ice initiation

A run was performed with all processes of ice formation excluded (the no-glaciation case) from the TOGA control. In the layer between −32° and −36°C, mean values of supercooled liquid water content at cloudy points (defined as in Fig. 6) were in the range of 0.2–0.3 g m^{-3} at all vertical velocities between 0.01 and 10 m s^{-1}, in the no-glaciation case. The threshold behavior of the supply of cloud liquid to the level of homogeneous droplet freezing, which was found in the TOGA control (Fig. 7), is totally absent in the no-glaciation case. Also, all cloudy points are close to water saturation ($-1 < s < 3\%$) in the no-glaciation case, in contrast with the subsaturation in the TOGA control (Fig. 6a). Consequently, the restriction of homogeneous droplet freezing to deep convective updrafts in the TOGA control is explicable in terms of vapor growth of preexisting ice causing total evaporation of the supercooled cloud liquid in regions of weak ascent (<1–2 m s^{-1}).

e. Correction applied to homogeneous aerosol freezing

In the light of recent experimental uncertainty about whether to apply a correction observed with the AIDA cloud chamber for the critical saturation ratio of −30% in the homogeneous freezing of ammonium sulfate aerosol (see section 2f), a run is performed with this correction included.

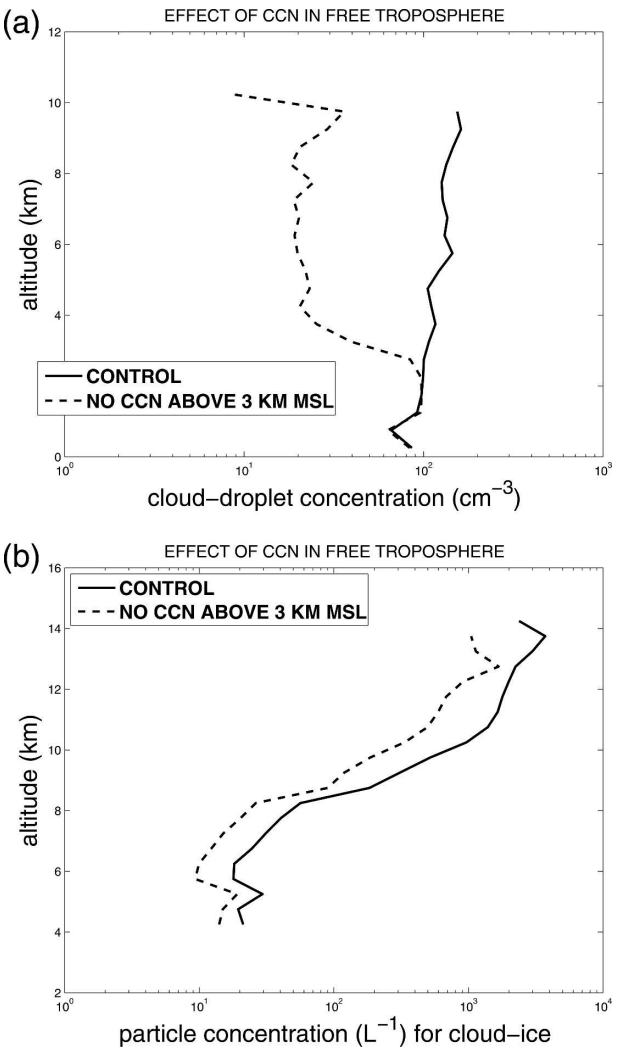

FIG. 9. Number concentration of (a) cloud droplets and (b) cloud ice from a simulation without CCN in the free troposphere, and the TOGA control. Model data are averaged in the same manner as for Fig. 2.

The average concentration of cloud ice is increased by about 30% in this run at most subzero levels relative to the TOGA control. Clearly episodes of homogeneous aerosol freezing become more frequent when the correction is included.

f. Droplet nucleation: CCN in the free troposphere

To assess the impact of CCN from the remote free troposphere on droplet nucleation, a run was performed without CCN ($C = 0$) in the cloud-free environment above 3 km MSL (the no-CCN/TOGA case).

Figure 9 shows that the average droplet concentration is reduced by almost one order of magnitude at all levels above 4 km MSL in the no-CCN/TOGA case

relative to the TOGA control. This is because the only source of CCN in the free troposphere is detrainment of boundary layer air from deep convective updrafts in the no-CCN/TOGA case. The number of CCN available for droplet formation in stratiform cloud and deep convective cores is then dramatically reduced. The ice concentration at all subzero levels is reduced by up to half of an order of magnitude in the no-CCN/TOGA case relative to the TOGA control, since homogeneous freezing of both aerosols and droplets is suppressed. Summed over the whole domain and duration of the no-CCN/TOGA case, the total numbers of aerosols and droplets that are frozen homogeneously are 98% and 70% lower, respectively, than in the TOGA control.

This critical dependence of crystal numbers aloft on CCN in the free troposphere is qualitatively consistent with simulations of individual cells of deep convection over Florida by Fridlind et al. (2004), Phillips et al. (2005), and Heymsfield et al. (2005): midtropospheric CCN are entrained into deep convective updrafts where they may be activated as cloud droplets that then freeze homogeneously, if upwelled far enough. The effect of midtropospheric CCN is rendered less dramatic in the cloud ensemble simulations by detrainment from deep convection of CCN from the boundary layer, which are then reentrained into deep convective towers.

On the scale of a cloud ensemble, CCN from the remote free troposphere are crucial for homogeneous aerosol freezing, which determines the concentrations of crystals over ubiquitous regions of weak ascent in the TOGA control. Finally, the averages of ice diameter are increased by up to about 5–10 μm below 11 km MSL (−43°C) because of the paucity of homogeneous ice and boosted growth rates, relative to the TOGA control.

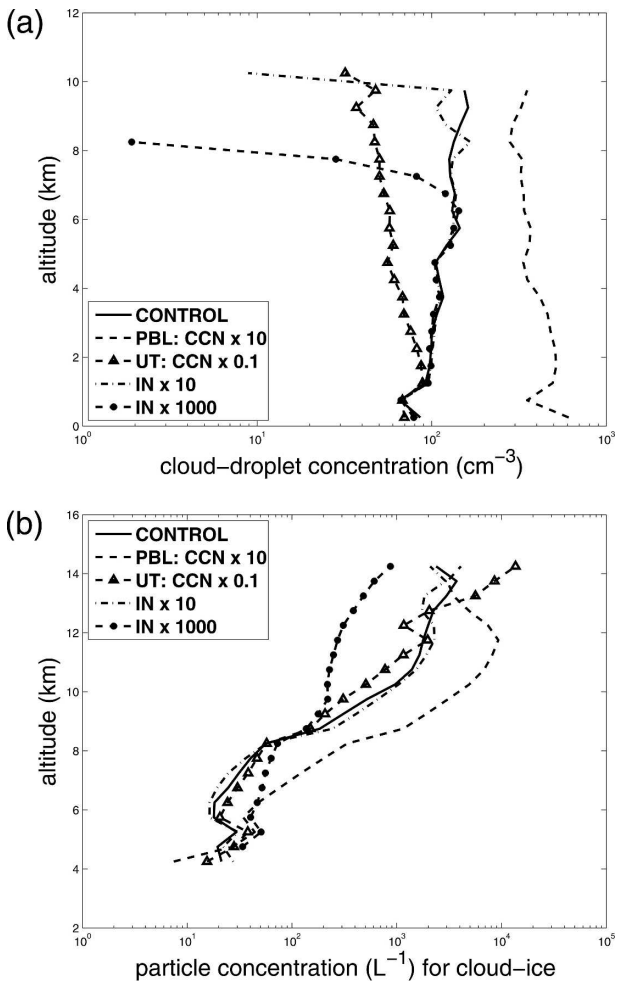

FIG. 10. Number concentration of (a) cloud droplets and (b) cloud ice from simulations of TOGA COARE with the environmental CCN concentration multiplied by factors of 10 in the PBL and 0.1 at 10–14 km MSL (UT), and with the IN concentration increased by factors of 10 and 1000, relative to the TOGA control. Model data are averaged in the same manner as for Fig. 2.

g. Sensitivity to aerosol concentrations

To explore impacts from the aerosol population, runs were made with the environmental CCN concentration multiplied by factors of 10 in the planetary boundary layer (the continental PBL/TOGA case) and 0.1 at 10–14 km MSL [the continental upper-tropospheric (UT)/TOGA case], and with the IN concentration increased by factors of 10 (the high-IN/TOGA case) and 1000 (the extreme IN/TOGA case). All these runs were compared with the TOGA control. In both continental PBL and UT/TOGA cases, the CCN concentration in the midtroposphere differs from the TOGA control as it is logarithmically interpolated over height between the boundary layer and 10 km MSL. The continental UT/TOGA case has been designed with a lower CCN concentration at upper levels than in the TOGA control because CCN concentrations aloft observed in the upper troposphere over the tropical Pacific are typically higher than over most continental regions (Clarke and Kapustin 2002).

Figure 10 shows that the continental PBL/TOGA case has a droplet concentration that is between 0.3 and 1 orders of magnitude higher than in the TOGA control throughout the mid and lower troposphere, because of the high numbers of soluble aerosols. Consequently, the ice concentration is about half an order of magnitude higher in the continental PBL/TOGA case at most subzero levels, with the total number of homogeneously frozen droplets being tripled when summed over the entire domain relative to the TOGA control. The corresponding total number of homogeneously fro-

zen aerosols is halved. The sensitivity from changes in CCN in the upper troposphere is less marked. The ice concentration in the continental UT/TOGA case is up to 50% lower at 8–12 km MSL (about −20° to −50°C) because of fewer supercooled droplets available for homogeneous freezing, but is up to half an order of magnitude higher above 13 km MSL (about −60°C) as homogeneous aerosol freezing is more prolific relative to the TOGA control.

Concentrations of cloud ice and droplets in the high-IN/TOGA case are quite similar to those in the TOGA control. However, in the extreme IN/TOGA case, which has IN concentrations typical of a desert dust episode (e.g., 28 July 2002, CRYSTAL-FACE), there are no droplets above the 8 km MSL (about −20°C) level. Vapor growth of the copious primary crystals causes complete evaporation of cloud liquid there, shutting down homogeneous droplet freezing and reducing the total numbers of aerosols frozen homogeneously throughout the whole domain by 95%. Consequently, the ice concentration above 8 km MSL is reduced by up to 1 order of magnitude, being increased by up to half an order of magnitude below this level.

6. Roles of nucleation processes in KWAJEX

Sensitivity tests are performed for the WRF simulation of KWAJEX (the KWAJEX control) to assess the role of nucleation processes. Vertical profiles presented here are again conditional averages over regions of visible cloud.

a. Homogeneous and heterogeneous ice nucleation

Four simulations were performed with the exclusion from the KWAJEX control run of homogeneous freezing of aerosols (the no-homogeneous aerosol freezing/KWAJEX case), cloud droplets (the no-homogeneous droplet freezing/KWAJEX case), and all particles (the no-homogeneous freezing/KWAJEX case), as well as a run without any heterogeneous nucleation (the no-heterogeneous freezing/KWAJEX case).

Figure 11 shows a reduction by over 2 orders of magnitude at most subzero levels above 8 km MSL (about −20°C) in the no-homogeneous freezing/KWAJEX case relative to the KWAJEX control. Homogeneous freezing of droplets and aerosols determines the average ice concentration aloft on the few occasions when upper-level cirrus forms. This behavior qualitatively resembles that found in the corresponding test for TOGA COARE (section 5). However, a unique feature of the KWAJEX simulations is that the infrequency of homogeneous freezing allows the HM process to dominate

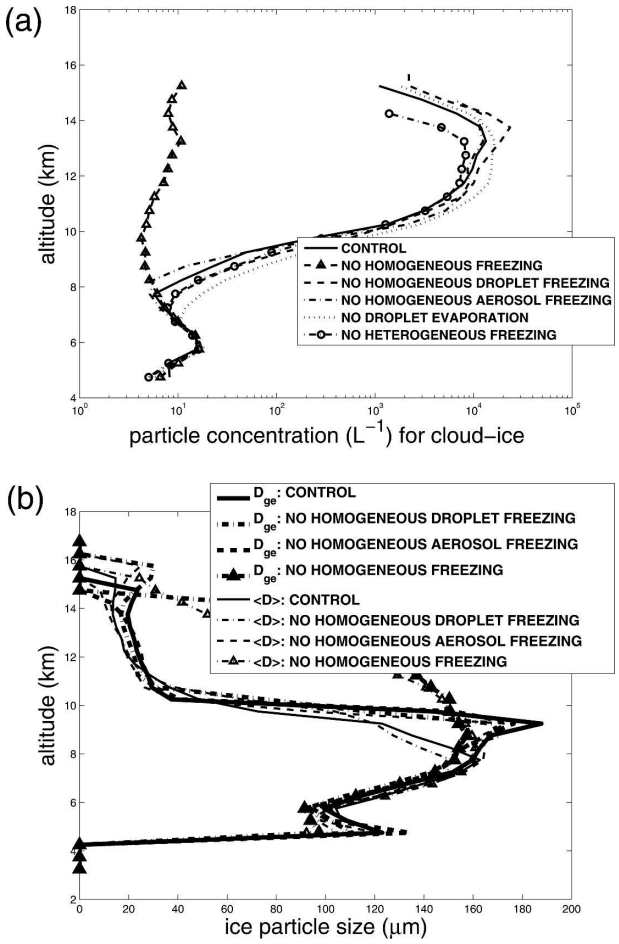

FIG. 11. (a) Number concentration and (b) size of cloud ice particles from the KWAJEX control and from corresponding simulations without homogeneous freezing of aerosols, droplets, and all liquid particles (aerosols, droplets, and rain) and without all heterogeneous freezing. Model data are averaged in the same manner as for Fig. 2.

the ice concentration throughout most of the mixed-phase region (5–10 km MSL; 0° to −36°C), causing a lack of sensitivity of the ice concentration there in these tests. The peak concentration of HM splinters is limited by the availability of supercooled cloud-liquid, which depends on the updraft speed (e.g., Heymsfield et al. 2005), which accounts for this insensitivity.

The infrequency of homogeneous freezing during the KWAJEX simulations is due to deep convection generally being shallower than in TOGA COARE. Cloud tops were mostly below 10 km MSL (−33°C) and upper-level cirrus was usually absent in KWAJEX (Heymsfield et al. 2002).

b. Secondary ice production

A run was made with the HM process of ice particle multiplication excluded (the no-HM/KWAJEX case)

from the KWAJEX control. Figure 12 shows that at subzero levels below about 7 km MSL (−11°C) there is a reduction by about 1 order of magnitude in the average concentration of cloud ice when the HM process is prohibited. Clearly, HM splinters govern the ice concentration throughout most of the mixed-phase region in the KWAJEX control, boosting it by up to an order of magnitude above the concentration of active IN (Fig. 1).

The HM process is particularly important in KWAJEX because there is a lack of upper-level cirrus from which homogeneous ice can descend toward the freezing level, as noted above. The response found in this test would be even more visible were it not for a compensating response in the no-HM/KWAJEX case, involving higher concentrations of homogeneous ice that fall out through the mixed-phase region relative to the KWAJEX control.

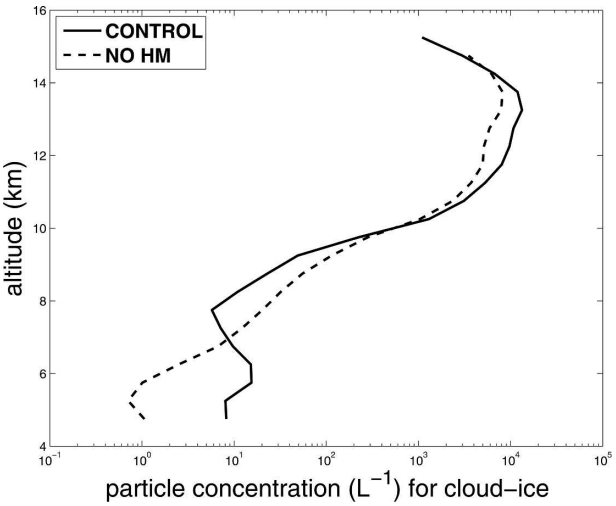

FIG. 12. Number concentration of cloud ice particles from a simulation with HM process of ice particle multiplication prohibited from the KWAJEX control. Model data are averaged in the same manner as for Fig. 2.

c. *Droplet nucleation: CCN in the free troposphere*

A run was performed without CCN ($C = 0$) in the cloud-free environment above 3 km MSL (the no-CCN/KWAJEX case) and compared with the KWAJEX control. The response found in this test is qualitatively similar to that found for TOGA COARE. The concentration of supercooled droplets is reduced throughout the mixed-phase region by between 0.5 (4 km MSL) and 1 (10 km MSL; −33°C) orders of magnitude, with the reduction becoming more marked with increasing height in the no-CCN/KWAJEX case relative to the KWAJEX control. There is a corresponding reduction in the number concentration of ice by one order of magnitude above 10 km MSL and by about half an order of magnitude at levels in the mixed-phase region. Homogeneous aerosol freezing is virtually eliminated, as was found in the corresponding test for TOGA COARE. The total number, summed over the entire domain, of homogeneously frozen droplets is reduced by over 90% in the no-CCN/KWAJEX case relative to the KWAJEX control.

7. Conclusions

This study has assessed the relative roles of nucleation processes for the generation of particles in a cloud ensemble simulated by a CSRM with double-moment bulk microphysics for two cases of deep convection in the tropical west Pacific region. The simulations of both cases have been compared extensively with available aircraft and satellite observations. Qualitative features, and some quantitative aspects, of these observations are reproduced by the model. The main conclusions are summarized as follows:

- Homogeneous freezing of activated cloud droplets at about −36°C, and of aerosols at colder temperatures than this, produce the vast majority of crystals in the domain. Homogeneously frozen particles descend into the mixed-phase region, dominating the average ice concentration at most subzero levels.
- Vertical velocities <1–2 m s^{-1} are associated with almost no supercooled cloud droplets reaching the −36°C level of homogeneous freezing, due to the vapor growth of preexisting ice. Homogeneous aerosol freezing occurs only in ubiquitous regions of weak ascent <1 and ≥0.05 m s^{-1}. In stronger updrafts, homogeneous droplet freezing occurs and the supersaturation is prevented from reaching the high values required for homogeneous aerosol freezing. If the ascent is too weak, <~0.05 m s^{-1}, preexisting ice similarly acts to inhibit homogeneous aerosol freezing.
- Preferential evaporation of small droplets during homogeneous droplet freezing, which has not been parameterized in any previous bulk microphysics scheme in the literature, produces a major impact on the domain-wide ice concentration when deep convection is vigorous. In the TOGA COARE simulation, its inclusion reduces the ice concentration by half an order of magnitude over a 2-km layer around the −36°C level.
- CCN concentrations in the free troposphere are crucial for determining in-cloud concentrations of supercooled droplets and concentrations of ice particles aloft formed by homogeneous freezing.
- Variations in the environmental CCN concentration, comparable with the difference between maritime

and continental regions, can produce order-of-magnitude impacts on the concentrations of cloud ice and droplets. Extra CCN in the mid- and lower troposphere cause higher concentrations of supercooled droplets to be supplied for homogeneous freezing, modifying homogeneous aerosol freezing.

- Extremely high concentrations of IN, typifying plumes of dust transported from desert regions, are found to modify the order of magnitude of ice and droplet concentrations. Supercooled cloud liquid in the upper half of the mixed phase region then is completely eliminated (e.g., by evaporation) in deep convective updrafts, shutting down the process of homogeneous droplet freezing. Homogeneous freezing of aerosols is also quenched. Similarly, previous studies of cirrus in the literature have shown the potential for competition between heterogeneous and homogeneous nucleation of crystals (e.g., Heymsfield and Sabin 1989; De Mott et al. 1997; Spice et al. 1999).
- Heterogeneous nucleation of cloud ice has an indirect impact on the domain-wide ice concentration, through its modification of rates of crystal production by homogeneous freezing. The domain-wide concentration of heterogeneous particles, and their HM splinters, is orders of magnitude lower than that of crystals formed by homogeneous freezing at most subzero levels, owing to the paucity of IN compared to CCN. Condensation and deposition freezing is the pathway for formation of almost all of the heterogeneous ice in the domain, whereas contact nucleation produces little impact.
- The HM process of ice particle multiplication controls the domainwide crystal concentration in the lower half of the mixed-phase region, especially in situations (e.g., KWAJEX) when the deep convection is shallow and homogeneous freezing aloft is infrequent.
- Experimental uncertainty in the homogeneous freezing of ammonium sulfate aerosol changes the ice concentration by about 30% at most subzero levels.

This fundamental role of homogeneous freezing may be viewed as a consequence of the paucity of IN aerosols in the troposphere compared to CCN (Fig. 1). It is not a universal result for all cloud systems, however. Extremely high concentrations of IN, or an absence of any convection above the −36°C level, can both suppress homogeneous freezing.

Concerning nucleation in deep convective updrafts, the following findings in previous studies are corroborated and extended to an ensemble of deep convective elements. Homogeneous droplet freezing was found to be restricted to vertical velocities greater than a certain threshold, according to Heymsfield et al. (2005). The WRF simulations confirm that this is due to a similar threshold behavior, caused by preexisting ice, in the vertical supply of supercooled liquid. Vapor growth of preexisting ice causes total evaporation of the supercooled cloud liquid if the source of supersaturation from ascent is insufficient (i.e., $<$1–2 m s^{-1}), as Heymsfield et al. have suggested. The significance of a w-dependent process of preferential evaporation of smaller droplets during homogeneous freezing of cloud liquid, which was discovered by Heymsfield et al., is confirmed in the WRF simulations. The finding of Fridlind et al. (2004) about the impact of free-tropospheric CCN on crystal numbers in a fast-deep convective updraft is corroborated by the drastic reductions in numbers of homogeneously frozen droplets when these aerosols are excluded from WRF simulations of both TOGA COARE and KWAJEX.

On the scale of a cloud ensemble, the WRF simulations show that homogeneous aerosol freezing covers a much greater horizontal area than homogeneous droplet freezing, because the former process occurs over ubiquitous regions of weak ascent. Consequently, the number of aerosols frozen homogeneously is much greater than that of homogeneous frozen droplets in the TOGA COARE simulation. Homogeneous aerosol freezing provides a key mechanism for how CCN from the remote free troposphere can determine overall crystal numbers in the cloud ensemble. When the cloud ensemble is exposed to continental levels of CCN concentration in the lower and midtroposphere, an intensification of homogeneous droplet freezing accompanies a reduction in numbers of aerosols frozen homogeneously relative to the maritime situation. This interplay between two mechanisms of homogeneous freezing is what produces the order-of-magnitude impact on the ice concentration when CCN are made more prolific. The vapor growth of extra homogeneously frozen droplets, which must eventually reach quiescent regions of the upper troposphere, makes the critical supersaturation for homogeneous aerosol freezing less likely to be reached. In this sense, there is a competition between both mechanisms.

There are several key areas of uncertainty inherent in the design of this double-moment bulk microphysics scheme. Assumptions about the form of the particle size distribution are crucial. The intercept parameters, $n_{x,0}$, for the size distributions of snow and graupel are uncertain, and must vary with the slope parameters, λ_x (e.g., Heymsfield et al. 2002). The parameters, p_x, determining the form of the size distribution for cloud particles are uncertain, and must also vary with λ_x and temperature. The formulation of heterogeneous nucle-

ation is based on a very limited set of field observations. Ideally, physically based equations for heterogeneous nucleation, validated against field observations, would be utilized. The large-scale advection of aerosol into the domain has necessarily been omitted from this simulation, so that the evolution of the CCN content in the cloud-free environment is not predicted. At high supersaturations approaching 1% the power-law form of the activity spectrum for CCN [Eq. (10)] probably becomes inaccurate (e.g., Cohard and Pinty 2000). The present model framework does not account for vertical transport of dusty air from the boundary layer to subzero levels in deep convective updrafts and for the consequent enhancement of numbers of crystals nucleated heterogeneously. Concerning the TOGA COARE and KWAJEX simulations described here, however, the boundary layer was observed to be maritime with very low CCN concentrations, which suggests that it is unlikely to have contained high concentrations of dust. Finally, the shape and bulk density of particles of cloud ice, snow, and graupel have been prescribed in a simplified fashion, neglecting important dependences on particle size and ambient conditions. Refinements of the representation of microphysics in these areas could improve this scheme, which is computationally more efficient than spectral microphysics.

Morrison et al. (2005) have also developed a physically based parameterization for ice nucleation, which, like that described here, could be used with a fully interactive aerosol component within a double-moment framework. As nucleation schemes are evaluated using observations, future development may focus on aerosol composition, including sea salt and organic aerosols. Indeed, parameterizations for droplet nucleation based on multiple aerosol species have recently been formulated by Ming et al. (2006) and Nenes and Seinfeld (2003). There is the prospect of including such schemes to represent the coupling between aerosols, chemistry, and clouds. The development of deep convection parameterizations that provide vertical velocity information (e.g., Donner 1993) open up the possibility of incorporating streamlined representations of limited double-moment bulk microphysics, so as to represent the outflow of particle numbers to cirrus and rates of convective precipitation in global models.

The insight afforded by sensitivity studies with WRF was limited by compensation among other microphysical processes when a given process was excluded. A more promising approach for further investigations would be to tag microphysical species according to their nucleation source with optional tracers. Finally, KWAJEX, CEPEX, and TOGA COARE yielded different aspects of the observational picture, with none of these being comprehensive. Consequently, uncertainties arose in the comparison of the model with observations. Clearly, simulations with advanced representations of cloud microphysics highlight the need for complete integration of aircraft, satellite and surface-based networks of observations within the same field experiment. It is essential that field campaigns include measurements of CCN and IN concentrations, which can have a high spatial and temporal variability.

Acknowledgments. The first author was funded by an award (NA17RJ2612) from the National Oceanic and Atmospheric Administration (NOAA), U.S. Department of Commerce. Statements, findings, conclusions, and recommendations are those of the authors and do not necessarily reflect the views of NOAA. Aircraft observations for TOGA COARE were provided by the Data Support Section of the Scientific Computing Division at NCAR. The authors are grateful to Aaron Bansemer, Greg McFarquhar, Jeff Stith, Paul DeMott, Bob Dattore, and Brad Ferrier for the valuable advice and data they provided.

APPENDIX

Linearized Supersaturation Scheme

This linearized scheme predicts the supersaturation and the diffusional growth of all species of hydrometeors. The equations for the evolution of the vapor mixing ratio, q, and temperature, T, are

$$\begin{cases} \dfrac{\partial q}{\partial t} = F_q - r_{\text{liq}}(q/q_{s,w} - 1) - r_{\text{ice}}(q/q_{s,i} - 1) \\ \dfrac{\partial T}{\partial t} = F_T + (L_v/c_p)r_{\text{liq}}(q/q_{s,w} - 1) + (L_s/c_p)r_{\text{ice}}(q/q_{s,i} - 1) \end{cases}. \tag{A1}$$

Here, the terms involving the phase transition rates, $r_{\text{liq}} \equiv r_w + r_r$ and $r_{\text{ice}} \equiv r_i + r_s + r_g$, are sinks of vapor associated with diffusional growth of hydrometeors (Ferrier 1994). They include size-dependent ventilation factors for drops (Pruppacher and Klett 1997) and ice (Hall and Pruppacher 1976). Also, F_q and F_T are the

sources of mixing ratio and temperature due to advection and all physical processes other than diffusional growth, while $q_{s,w}$ and $q_{s,i}$ are the saturation mixing ratios with respect to liquid water and ice, respectively. Also, L_v and L_s are the latent heats of evaporation and sublimation.

These two evolution equations are written in terms of perturbations of q and T from their values, q_0 and T_0, at the start of the time step, Δt. The evolution equations are linearized, with Taylor expansions of $q_{s,w}$ and $q_{s,i}$ to first order with respect to T, and are expressed in matrix form:

$$\frac{\partial \mathbf{V}}{\partial t} \approx \mathbf{M}\mathbf{V} + \mathbf{h},$$

where $\mathbf{V}(t) = [q' \quad T']$ and

$$\mathbf{h} = \begin{bmatrix} F_q - q_0\left(\dfrac{r_{\text{liq}}}{q_{s,w,0}} + \dfrac{r_{\text{ice}}}{q_{s,i,0}}\right) + r_{\text{liq}} + r_{\text{ice}} \\ F_T + q_0\left\{\dfrac{(L_v/c_p)r_{\text{liq}}}{q_{s,w,0}} + \dfrac{(L_s/c_p)r_{\text{ice}}}{q_{s,i,0}}\right\} - \{(L_v/c_p)r_{\text{liq}} + (L_s/c_p)r_{\text{ice}}\} \end{bmatrix},$$

while

$$\mathbf{M} = \begin{bmatrix} -\left(\dfrac{r_{\text{liq}}}{q_{s,w,0}} + \dfrac{r_{\text{ice}}}{q_{s,i,0}}\right) & \dfrac{r_{\text{liq}}q_0\Gamma_w}{q_{s,w,0}^2} + \dfrac{r_{\text{ice}}q_0\Gamma_i}{q_{s,i,0}^2} \\ \dfrac{(L_v/c_p)r_{\text{liq}}}{q_{s,w,0}} + \dfrac{(L_s/c_p)r_{\text{ice}}}{q_{s,i,0}} & -\left\{\dfrac{(L_v/c_p)r_{\text{liq}}q_0\Gamma_w}{q_{s,w,0}^2} + \dfrac{(L_s/c_p)r_{\text{ice}}q_0\Gamma_i}{q_{s,i,0}^2}\right\} \end{bmatrix}.$$

Here, $q_{s,w,0} = q_{s,w}(t = 0)$ and similarly for $q_{s,i,0}$. Now, $\mathbf{M}$ has eigenvectors, $\mathbf{x}_j$, and eigenvalues, λ_j, where $j = 1, 2$. The total loss of vapor from diffusional growth is $\Delta q_{\text{vap}} = q_0 + q'(\Delta t) - q^*$, where q^* is the hypothetical vapor mixing ratio at the end of the time step without diffusional growth. The analytical solution is $X'(t) = E_{X,1}(t) + E_{X,2}(t)$, where $X = q$, T (for $k = 1, 2$). For $\lambda_j \neq 0$, then $E_{X,j}(t) = A_{X,j}[\exp(\lambda_j t) - 1]$, where $A_{X,j} = x_k, {}_jR_j/\lambda_j$. For $\lambda_j = 0$, there is $E_{X,j} = x_{k,j}R_j\Delta t$. If only liquid is present, then the mass diffused onto liquid is $\Delta q_{\text{liq,diff}} = -\Delta q_{\text{vap}}$ (and similarly for $\Delta q_{\text{ice,diff}}$ when only ice being present).

When both liquid and ice are present, then the mass increments, $\Delta q_{\text{liq,diff}}$ and $\Delta q_{\text{ice, diff}}$, are obtained by substituting $q'(t)$ into the linearized terms for diffusional growth in the evolution equation for q and integration over Δt:

$$\Delta q_{x,\text{diff}} \approx \frac{r_x}{q_{s,x,0}}\left(C_q - \Delta t q_{s,x,0} + \Delta t q_0 - C_T\frac{\Gamma_x q_0}{q_{s,x,0}}\right),$$

where $x =$ liq, ice. Here, $C_X = D_{X,1} + D_{X,2}$. For $\lambda_j \neq 0$:

$$D_{X,j} = \int_0^{\Delta t} E_{X,j}(t)\,dt = A_{X,j}\frac{[\exp(\Delta t\lambda_j) - 1]}{\lambda_j} - A_{X,j}\Delta t.$$

If $\lambda_j = 0$, then $D_{X,j} = x_{k,j}R_j\Delta t^2/2$. The mass increment with the larger absolute magnitude is then adjusted such that $\Delta q_{\text{liq,diff}} + \Delta q_{\text{ice,diff}} = -\Delta q_{\text{vap}}$. Each mass increment is partitioned among individual species according to the ratios $r_w{:}r_r$ for liquid and $r_i{:}r_s{:}r_g$ for ice.

The scheme is implemented in WRF by subcycling over the WRF model's advective time step of 10 s. The frequency of subcycling increases with the local droplet concentration and cooling rate, F_T, so as to optimize accuracy. An offline validation of this linearized supersaturation scheme has been performed for 100 s of vapor growth, using a finite difference nonlinear scheme that solves the fully nonlinear evolution equations for q and T given above at extremely high resolution in time. No precipitation is present during this idealized test. The fractional error in the predicted supersaturation from the linearized supersaturation scheme described here is always less than about 0.02, for cooling rates corresponding to vertical velocities of adiabatic ascent ranging from 0.01 to 30 m s^{-1} and populations of droplets (at 10°C) or crystals (at −50°C) ranging from 0.01 to 1000 cm^{-3}.

Walko et al. (2000) have provided a scheme that differs from ours in that they solve numerically the implicit finite difference equations for mixing ratios. While their approach is stable at long time steps, our scheme obtains an accurate analytical solution of the evolution of mixing ratios and temperature during a time step.

REFERENCES

Auer, A. H., and D. L. Veal, 1970: The dimension of ice crystals in natural clouds. *J. Atmos. Sci.,* **27,** 919–926.

Baker, B. A., 1991: On the role of phoresis in cloud ice initiation. *J. Atmos. Sci.,* **48,** 1545–1548.

Bertram, A. K., T. Koop, L. T. Molina, and M. J. Molina, 2000: Ice

formation in (NH4)2SO4-H2O particles. *J. Phys. Chem. A,* **104,** 584–588.

Burks, J. E., 1998: Radiative fluxes and heating rates during TOGA COARE over the Intensive Flux Array. M.S. dissertation, Dept. of Meteorology, University of Utah, 85 pp.

Carstens, J. C., and J. J. Martin, 1982: In-cloud scavenging by thermophoresis, diffusiophoresis and Brownian diffusion. *J. Atmos. Sci.,* **39,** 1124–1129.

Chaumerliac, N., E. Richard, and J.-P. Pinty, 1987: Sulfur scavenging in a mesoscale model with quasi-spectral microphysics: Two-dimensional results for continental and maritime clouds. *J. Geophys. Res.,* **92,** 3114–3126.

Chen, J.-P., and S.-T. Liu, 2004: Physically based two-moment bulkwater parametrization for warm-cloud microphysics. *Quart. J. Roy. Meteor. Soc.,* **130,** 51–78.

Ciesielski, P. E., L. M. Hartten, and R. H. Johnson, 1997: Impacts of merging profiler and rawinsonde wins on TOGA COARE analyses. *J. Atmos. Oceanic Technol.,* **14,** 1264–1279.

Clarke, A. D., 1993: A global survey of atmospheric nuclei in the remote mid-troposphere: Their nature, concentration and evolution. *J. Geophys. Res.,* **98,** 20 633–20 647.

——, and V. N. Kapustin, 2002: A Pacific aerosol survey. Part I: A decade of data on particle production, transport, evolution and mixing in the troposphere. *J. Atmos. Sci.,* **59,** 363–382.

Cohard, J.-M., and J.-P. Pinty, 2000: A comprehensive two-moment warm microphysical bulk scheme. I: Description and tests. *Quart. J. Roy. Meteor. Soc.,* **126,** 1815–1842.

Cotton, W. R., G. J. Tripoli, R. M. Rauber, and E. A. Mulvihull, 1986: Numerical simulation of the effects of varying ice crystal nucleation rates and aggregation processes on orographic snowfall. *J. Climate Appl. Meteor.,* **25,** 1658–1680.

——, and Coauthors, 2003: RAMS 2001: Current status and future directions. *Meteor. Atmos. Phys.,* **82,** 5–29.

DeMott, P. J., D. C. Rogers, and S. M. Kreidenweiss, 1997: The susceptibility of ice formation in upper-tropospheric clouds to insoluble aerosol components. *J. Geophys. Res.,* **102,** 19 575–19 584.

——, D. J. Cziczo, A. J. Prenni, D. M. Murphy, S. M. Kreidenweis, D. S. Thomson, R. Borys, and D. C. Rogers, 2003: Measurements of the concentration and composition of nuclei for cirrus formation. *Proc. Natl. Acad. Sci. USA,* **100,** 14 655–14 660.

Donner, L. J., 1993: A cumulus parameterization including mass fluxes, vertical momentum dynamics, and mesoscale effects. *J. Atmos. Sci.,* **50,** 889–906.

——, C. J. Seman, and R. S. Hemler, 1999: Three-dimensional cloud-system modeling of GATE convection. *J. Atmos. Sci.,* **56,** 1885–1912.

Ferrier, B. S., 1994: A double-moment multiple-phase four-class bulk ice scheme. Part I: Description. *J. Atmos. Sci.,* **51,** 249–280.

Freidenreich, S. M., and V. Ramaswamy, 1999: A new multiple-band solar radiative parameterization for general circulation models. *J. Geophys. Res.,* **104,** 31 389–31 410.

Fridlind, A. M., and Coauthors, 2004: Evidence for the predominance of mid-tropospheric aerosols as subtropical anvil cloud nuclei. *Science,* **304,** 718–722.

Fu, Q., 1996: An accurate parameterization of the solar radiative properties of cirrus clouds for climate models. *J. Climate,* **9,** 2058–2082.

——, and K. N. Liou, 1993: Parameterization of the radiative properties of cirrus clouds. *J. Atmos. Sci.,* **50,** 2008–2025.

——, S. K. Krueger, and K. N. Liou, 1995: Interactions of radiation and convection in simulated tropical cloud clusters. *J. Atmos. Sci.,* **52,** 1310–1328.

——, P. Yang, and W. B. Sun, 1998: An accurate parameterization of the infrared radiative properties of cirrus clouds for climate models. *J. Climate,* **11,** 2223–2237.

Girard, E., and J. A. Curry, 2001: Simulation of Arctic low-level clouds observed during the FIRE Arctic Clouds Experiment using a new bulk microphysics scheme. *J. Geophys. Res.,* **106,** 15 139–15 154.

Hall, W. D., and H. R. Pruppacher, 1976: The survival of ice particles falling from cirrus clouds in subsaturated air. *J. Atmos. Sci.,* **33,** 1995–2006.

Hallett, J., and S. C. Mossop, 1974: Production of secondary ice particles during the riming process. *Nature,* **249,** 26–28.

Harrington, J. Y., M. P. Meyers, R. L. Walko, and W. R. Cotton, 1995: Parameterization of ice crystal conversion processes due to vapor deposition for mesoscale models using double-moment basis functions. Part I: Basic formulation and parcel model results. *J. Atmos. Sci.,* **52,** 4344–4366.

Held, I., R. S. Hemler, and V. Ramaswamy, 1993: Radiative–convective equilibrium with explicit two-dimensional moist convection. *J. Atmos. Sci.,* **50,** 3909–3927.

Heymsfield, A. J., and R. M. Sabin, 1989: Cirrus crystal nucleation by homogeneous freezing of solution droplets. *J. Atmos. Sci.,* **46,** 2252–2264.

——, A. Bansemer, P. R. Field, S. L. Durden, J. L. Stith, J. E. Dye, W. Hall, and C. Grainger, 2002: Observations and parameterizations of particle size distributions in deep tropical cirrus and stratiform precipitating clouds: Results from in situ observations in TRMM field campaigns. *J. Atmos. Sci.,* **59,** 3457–3491.

——, ——, C. Schmitt, C. Twohy, and M. R. Poellot, 2004: Effective ice particle densities derived from aircraft data. *J. Atmos. Sci.,* **61,** 982–1003.

——, L. M. Miloshevich, C. Schmitt, A. Bansemer, C. Twohy, M. R. Poellot, A. Fridlind, and H. Gerber, 2005: Homogeneous ice nucleation in subtropical and tropical convection and its influence on cirrus anvil microphysics. *J. Atmos. Sci.,* **62,** 41–65.

Hung, H.-M., A. Malinowski, and S. T. Martin, 2002: Ice nucleation kinetics of aerosols containing aqueous and solid ammonium sulfate particles. *J. Phys. Chem. A,* **106,** 293–306.

Ikawa, M., H. Mizuno, T. Matsuo, M. Murakami, Y. Yamada, and K. Saito, 1991: Numerical modeling of convective snow clouds over the Sea of Japan: Precipitation mechanisms and sensitivity to ice crystal nucleation rates. *J. Meteor. Soc. Japan,* **69,** 641–667.

Kajikawa, M., 1976: Observation of falling motion of columnar snow crystals. *J. Meteor. Soc. Japan,* **54,** 276.

Karcher, B., and U. Lohmann, 2002: A parameterization of cirrus cloud formation: Homogeneous freezing of supercooled aerosols. *J. Geophys. Res.,* **107,** 4010, doi:10.1029/2001JD000470.

Khairoutdinov, M. F., and Y. L. Kogan, 2000: A new cloud physics parameterization in a large-eddy simulation model of marine stratocumulus. *Mon. Wea. Rev.,* **128,** 229–243.

Koop, T., B. P. Luo, A. Tsias, and T. Peter, 2000: Water activity as the determinant for homogeneous ice nucleation in aqueous solutions. *Nature,* **406,** 611–614.

Kummerow, C., and Coauthors, 2000: The status of the Tropical Rainfall Measuring Mission (TRMM) after two years in orbit. *J. Appl. Meteor.,* **39,** 1965–1982.

Levkov, L., B. Rockel, H. Kapitza, and E. Raschke, 1992: 3D mesoscale numerical studies of cirrus and stratus clouds by their time and space evolution. *Beitr. Phys. Atmos.,* **65,** 35–58.

Lin, Y.-L., R. D. Farley, and H. D. Orville, 1983: Bulk parameterization of the snow field in a cloud model. *J. Climate Appl. Meteor.,* **22,** 1065–1092.

Lipps, F. B., and R. Hemler, 1986: Numerical simulation of deep tropical convection associated with large-scale convergence. *J. Atmos. Sci.,* **43,** 1796–1816.

Lord, S. J., H. E. Willoughby, and J. M. Piotrowicz, 1984: Role of a parameterized ice-phase microphysics in an axisymmetric nonhydrostatic tropical cyclone model. *J. Atmos. Sci.,* **41,** 2836–2848.

Mangold, A., R. Wagner, H. Saathoff, U. Schurath, C. Giesermann, V. Ebert, M. Kramer, and O. Mohler, 2005: Experimental investigation of ice nucleation by different types of aerosols in the aerosol chamber AIDA: Implications to microphysics of cirrus clouds. *Meteor. Z.,* **14,** 485–498.

McFarquhar, G. M., and A. J. Heymsfield, 1997: Parameterization of tropical cirrus ice crystal size distributions and implications for radiative transfer: Results from CEPEX. *J. Atmos. Sci.,* **54,** 2187–2200.

——, ——, A. Macke, J. Iaquinta, and S. M. Aulenbach, 1999: Use of observed ice crystal sizes and shapes to calculate mean-scattering properties and multispectral radiances: CEPEX April 4, 1993, case study. *J. Geophys. Res.,* **104,** 31 763–31 779.

Meyers, M. P., P. J. DeMott, and W. R. Cotton, 1992: New primary ice-nucleation parameterizations in an explicit cloud model. *J. Appl. Meteor.,* **31,** 708–720.

——, R. L. Walko, J. Y. Harrington, and W. R. Cotton, 1997: New RAMS cloud microphysics parameterization. Part II: The two-moment scheme. *Atmos. Res.,* **45,** 3–39.

Ming, Y., V. Ramaswamy, L. J. Donner, and V. T. J. Phillips, 2006: A new parameterization of cloud droplet activation applicable to general circulation models. *J. Atmos. Sci.,* **63,** 1348–1356.

Minnis, P., W. L. Smith, D. P. Garber, J. K. Ayers, and D. R. Doelling, 1995: Cloud properties derived from GOES-7 for spring 1994 ARM intensive observation period using version 1.0.0 of ARM satellite data analysis program. NASA Reference Publication 1366, 59 pp.

Morrison, H., J. A. Curry, and V. I. Khvorostyanov, 2005: A new double-moment microphysics parameterization for application in cloud and climate models. Part I: Description. *J. Atmos. Sci.,* **62,** 1665–1677.

Nenes, A., and J. H. Seinfeld, 2003: Parameterization of cloud droplet formation in global climate models. *J. Geophys. Res.,* **108,** 4415, doi:10.1029/2002JD002911.

Ono, A., 1969: The shape and riming properties of ice crystals in natural clouds. *J. Atmos. Sci.,* **26,** 138–147.

Ovtchinnikov, M., Y. L. Kogan, and A. M. Blyth, 2000: An investigation of ice production mechanisms in small cumuliform clouds using a 3D model with explicit microphysics. Part II: Case study of New Mexico cumulus clouds. *J. Atmos. Sci.,* **57,** 3004–3020.

Pawlowska, H., and J. L. Brenguier, 2000: The indirect effect of aerosol on climate: Effect of aerosol properties on precipitation efficiency. *Proc. 13th Int. Conf. on Clouds and Precipitation,* Reno, NV, ICCP, 856–859.

Phillips, V. T. J., and L. J. Donner, 2007: Cloud microphysics, radiation and dynamics in two- and three-dimensional simulations of deep convection. *Quart. J. Roy. Meteor. Soc.,* in press.

——, and Coauthors, 2005: Anvil glaciation in a deep cumulus updraft over Florida simulated with an Explicit Microphysics Model. I: The impact of various nucleation processes. *Quart. J. Roy. Meteor. Soc.,* **131,** 2019–2046.

Prenni, A. J., M. E. Wise, S. D. Brooks, and M. A. Tolbert, 2001: Ice nucleation in sulfuric acid and ammonium sulfate particles. *J. Geophys. Res.,* **106,** 3037–3044.

Pruppacher, H. R., and J. D. Klett, 1997: *Microphysics of Clouds and Precipitation.* Kluwer Academic, 954 pp.

Reisner, J., R. M. Rasmussen, and R. T. Bruintjes, 1998: Explicit forecasting of supercooled liquid water in winter storms using the MM5 mesoscale model. *Quart. J. Roy. Meteor. Soc.,* **124,** 1071–1108.

Rogers, R. R., and M. K. Yau, 1991: *A Short Course in Cloud Physics.* Pergamon Press.

Rossow, W. B., and Y.-C. Zhang, 1995: Calculation of surface and top of atmosphere radiative fluxes from physical quantities based on ISCCP datasets. 2. Validation and first results. *J. Geophys. Res.,* **100,** 1167–1197.

Saleeby, S. M., and W. R. Cotton, 2004: A large-droplet mode and prognostic number concentration of cloud droplets in the Colorado State University Regional Atmospheric Modeling System (RAMS). Part I: Module descriptions and supercell test simulations. *J. Appl. Meteor.,* **43,** 182–195.

Savijarvi, H., 1997: Short-wave optical properties of rain. *Tellus,* **49A,** 177–181.

Schwarzkopf, M. D., and V. Ramaswamy, 1999: Radiative effects of CH4, N2O halo-carbons and the foreign-broadened H2O continuum: A GCM experiment. *J. Geophys. Res.,* **104,** 9467–9488.

Seifert, A., and K. D. Beheng, 2005: A two-moment cloud microphysics parameterization for mixed-phase clouds. Part 1: Model description. *Meteor. Atmos. Phys.,* **92,** 45–66.

Slingo, A., 1989: A GCM parameterization for the shortwave radiative properties of water clouds. *J. Atmos. Sci.,* **46,** 1419–1427.

Spice, A., D. W. Johnson, P. R. A. Brown, A. G. Darlinson, and C. P. R. Saunders, 1999: Heterogeneous droplet freezing in orographic cirrus clouds: A numerical simulation of the microphysics. *Quart. J. Roy. Meteor. Soc.,* **125,** 1637–1667.

Spracklen, D. V., K. J. Pringle, K. S. Carslaw, M. P. Chipperfield, and G. W. Mann, 2005: A global off-line model of size-resolved aerosol microphysics: I. Model development and prediction of aerosol properties. *Atmos. Chem. Phys. Discuss.,* **5,** 179–215.

Swann, H., 1998a: *A Description of the Three-Phase Double-Moment Bulk-Water Microphysics Scheme Used in the Large-Eddy Model.* Meteorological Office, Bracknell, United Kingdom.

——, 1998b: Sensitivity to the representation of precipitating ice in CRM simulations of deep convection. *Atmos. Res.,* **47,** 415–435.

Tampieri, F., and C. Tomasi, 1976: Size distribution models of fog and cloud droplets in terms of the modified gamma function. *Tellus,* **28,** 333–347.

Tripoli, G. J., and W. R. Cotton, 1980: A numerical investigation of several factors contributing to the observed variable intensity of deep convection over South Florida. *J. Appl. Meteor.,* **19,** 1037–1063.

Twomey, S., 1959: The nuclei of natural cloud formation: The supersaturation in natural clouds and the variation of cloud droplet concentration. *Geofis. Pura Appl.,* **43,** 243–249.

——, 1966: Computations of rain formation by coalescence. *J. Atmos. Sci.,* **23,** 405–411.

Walko, R. L., W. R. Cotton, M. P. Meyers, and J. Y. Harrington, 2000: Efficient computation of vapor and heat diffusion between hydrometeors in a numerical model. *Atmos. Res.,* **53,** 171–183.

Wang, C., and J. S. Chang, 1993: A three-dimensional model of cloud dynamics, microphysics and chemistry: 1. Concepts and formulation. *J. Geophys. Res.,* **98,** 14 827–14 844.

Weller, R. A., and S. P. Anderson, 1996: Surface meteorology and air–sea fluxes in the western equatorial Pacific warm pool during the TOGA Coupled Ocean–Atmosphere Response Experiment. *J. Climate,* **9,** 1959–1990.

Young, K. C., 1974: The role of contact nucleation in ice phase initiation. *J. Atmos. Sci.,* **31,** 768–776.

Zhang, M. H., J. L. Lin, R. T. Cederwall, J. J. Yio, and S. C. Xie, 2001: Objective analysis of the ARM IOP data: Method and sensitivity. *Mon. Wea. Rev.,* **129,** 295–311.

Zhang, Y.-C., W. B. Rossow, and A. A. Lacis, 1995: Calculation of surface and top of atmosphere radiative fluxes from physical quantities based on ISCCP datasets. 1. Method and sensitivity to input data uncertainties. *J. Geophys. Res.,* **100,** 1149–1166.

Ziegler, C. L., 1985: Retrieval of thermal and microphysical variables in observed convective storms. Part I: Model development and preliminary testing. *J. Atmos. Sci.,* **42,** 1487–1509.